# 2

# Thermal remote sensing of active volcanism: principles

The physical basis of thermal remote sensing of active volcanoes is the Planck Function. An understanding of this function allows any methodology applied in this book to be understood, adapted and applied. We thus focus here on the application of the Planck Function, as well as complications when using the function to deal with at-sensor spectral thermal radiance emitted by a graybody source located on the Earth's surface. Example images, and pictures of the surface types, to which we apply these principles are given later in the book (especially across Chapters 4, 6 and 9, as well as in Electronic Supplement 1).

## 2.1 The Planck Function, Wein's Displacement Law and Stefan–Boltzmann

In this book we use the nomenclature defined for all radiative terms by the *Manual of Remote Sensing* (Janza *et al.*, 1975). These definitions are given in Table 2.1. We first deal with spectral radiant exitance from the radiator which, in our case, is the Earth's surface. Published by Max Planck in 1901, the Planck Function describes how spectral radiant exitance, $M(\lambda,T)$, from a blackbody varies with temperature ($T$) and wavelength ($\lambda$). The function is given by:

$$M(\lambda, T) = 2\pi hc^2\lambda^{-5}\left[\exp^{\frac{hc}{\lambda kT}} - 1\right]^{-1} \left(\mathrm{W\,m^{-2}\,m^{-1}}\right) \tag{2.1a}$$

in which $h$ is Planck's constant ($6.6256 \times 10^{-34}$ J s), $c$ is the speed of light ($2.9979 \times 10^{8}$ m s$^{-1}$), and $k$ is the Boltzmann gas constant ($1.38 \times 10^{-23}$ J K$^{-1}$). Because temperature and wavelength are the only variables, Equation (2.1a) can be simplified by combining the constants that contribute to the first and second terms of (2.1a), so that:

$$c_1 = 2\pi hc^2 = 3.741 \times 10^{-16}\ \mathrm{W\,m^2}$$

and

$$c_2 = hc/k = 1.4393 \times 10^{-2}\ \mathrm{m\,K}.$$

Table 2.1. *Summary and definition of radiative terms [modified from Table 3–3 of Suits et al. (1975)].*

| Name | Symbol | Units | Definition |
|---|---|---|---|
| Radiant energy | $Q_{rad}$ | Joules (J) | Capacity of radiation (integrated across a given spectral band) to do work. |
| Radiant flux | $\Phi_{rad}$ | Watts ($W = J\ s^{-1}$) | Time rate of radiative energy flow on to, or off of, a surface. |
| Radiant flux density | $M_{rad}$ | Watts per square meter ($W\ m^{-2}$) | Time rate of radiative energy flow on to, or off of, a surface per unit area of that surface. |
| | | Radiant flux density at the surface | |
| Irradiance | $E$ | Watts per square meter ($W\ m^{-2}$) | Radiant flux incident upon a surface per unit area of that surface. |
| Radiant exitance | $M$ | Watts per square meter ($W\ m^{-2}$) | Radiant flux leaving a surface per unit area of that surface. |
| Radiant intensity | $I$ | Watts per steradian ($W\ sr^{-1}$) | Radiant flux leaving a small source per unit solid angle in a specified direction. |
| Radiance | $L$ | Watts per steradian per square meter ($W\ sr^{-1}\ m^{-2}$) | Radiant intensity per unit area of a small source per unit solid angle. |

Note.
Adding the term "spectral" before each term means that the measurement is a spectral quantity. That is, it is measured at a particular wavelength ($\lambda$). In this case, the quantity becomes a function of $\lambda$, and the measurement is thus given per unit wavelength. Radiant exitance, for example, becomes:

Spectral radiant exitance: $M(\lambda)$ in Watts per square meter per micron ($W\ m^{-2}\ \mu m^{-1}$). That is, radiant flux leaving a surface per unit area of that surface, measured per unit wavelength.

This allows a simplified version of (2.1a) to be written:

$$M(\lambda, T) = c_1 \lambda^{-5} \left[ \exp^{\frac{c_2}{\lambda T}} - 1 \right]^{-1} \qquad \left(W\ m^{-2}\ m^{-1}\right). \tag{2.1b}$$

Dividing the result by $10^{-6}$ gives spectral radiant exitance in the more commonly used units of watts per meter squared per micron ($W\ m^{-2}\ \mu m^{-1}$).

If we hold the temperature of the emitting body constant, the Planck Function can be used to show how spectral radiant exitance from a blackbody varies with wavelength. The resulting Planck curves for a series of typical ambient and active lava temperatures are plotted in Figure 2.1. The plot illustrates three key principles.

(1) Planck curves for two blackbodies at two different temperatures will not cross.
(2) In the shortwave infrared, spectral radiant exitance from blackbodies at ambient temperature becomes very small.

Table 2.2. *Spectral exitance at 1.1 μm, 2.5 μm, 3.5 μm, 10 μm and 12 μm for blackbodies at a range of Earth ambient and lava temperatures, with wavelength of peak emission for each temperature.*

| Blackbody temperature (°C) | Spectral exitance (W $m^{-2}$ $m^{-1}$) | | | | | Wavelength of peak emission (μm) |
|---|---|---|---|---|---|---|
| | 1.1 μm | 2.5 μm | 3.5 μm | 10 μm | 12 μm | |
| −50 | 7.96E−12 | 2.39E+01 | 7.07E+03 | 5.92E+06 | 7.00E+06 | 13.0 |
| 0 | 3.65E−07 | 2.69E+03 | 2.06E+05 | 1.94E+07 | 1.89E+07 | 10.6 |
| 50 | 6.04E−04 | 7.01E+04 | 2.12E+06 | 4.40E+07 | 3.77E+07 | 9.0 |
| 100 | 1.37E−01 | 7.63E+05 | 1.17E+07 | 8.07E+07 | 6.29E+07 | 7.8 |
| 250 | 3.19E+03 | 6.37E+07 | 2.75E+08 | 2.55E+08 | 1.69E+08 | 5.5 |
| 500 | 1.04E+07 | 2.24E+09 | 3.51E+09 | 6.88E+08 | 4.04E+08 | 3.7 |
| 800 | 1.18E+09 | 1.80E+10 | 1.58E+10 | 1.32E+09 | 7.31E+08 | 2.7 |
| 1000 | 7.99E+09 | 4.21E+10 | 2.93E+10 | 1.78E+09 | 9.60E+08 | 2.3 |
| 1100 | 1.69E+10 | 5.88E+10 | 3.75E+10 | 2.02E+09 | 1.08E+09 | 2.1 |
| 1200 | 3.23E+10 | 7.85E+10 | 4.65E+10 | 2.26E+09 | 1.20E+09 | 2.0 |

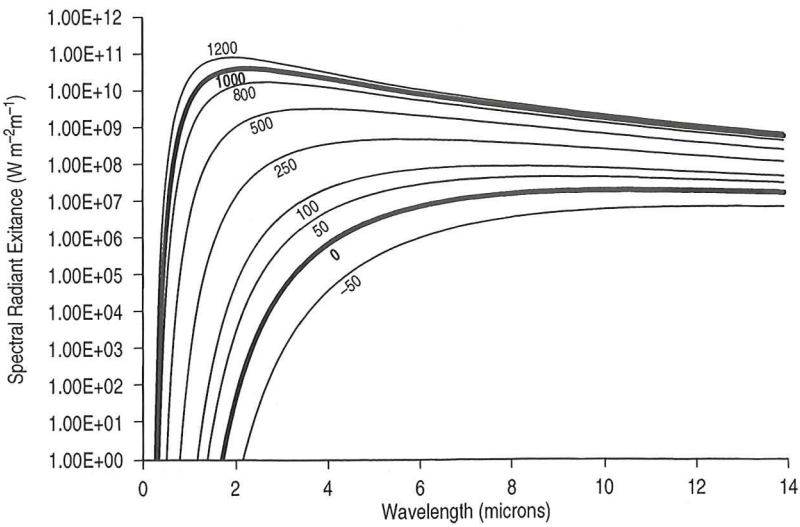


Figure 2.1 Planck curves plotted using Equation (2.1b) for blackbody surfaces at temperatures between −50 °C and 1200 °C.

(3) Spectral radiant exitance for a high-temperature blackbody is greater than that for a low-temperature blackbody at all wavelengths, but the difference is greatest in the shortwave infrared and least in the thermal infrared.

These three principles mean that, as detailed in Table 2.2, the following rules apply.

- At 1.1 μm, spectral radiant exitance from a blackbody at ambient temperature (0 °C) is small. However, exitance for a blackbody at magmatic temperature (1000 °C) is 16 orders of magnitude larger.

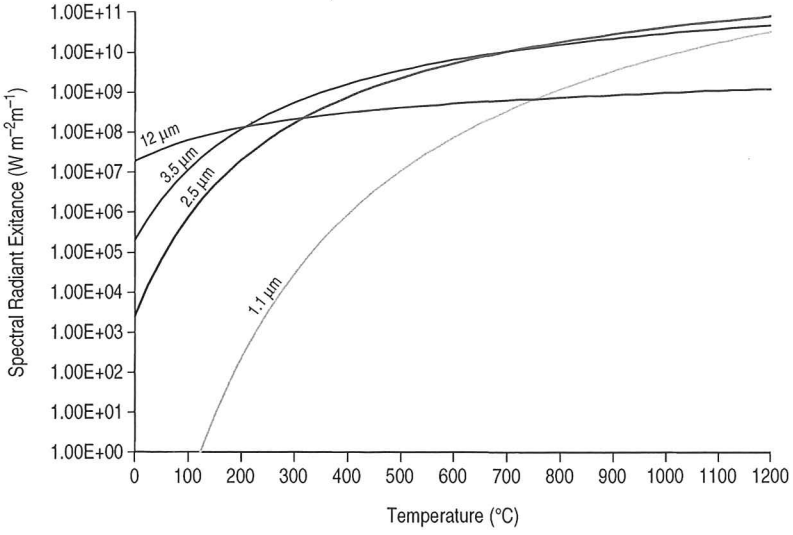


Figure 2.2 Increase in spectral radiant exitance with temperature for a blackbody surface emitting in the NIR (at 1.1 μm), SWIR (at 2.5 μm), MIR (at 3.5 μm) and TIR (at 12 μm).

- Between 1.1 μm and 3.5 μm, spectral radiant exitance from the blackbody at 0 °C increases by 12 orders of magnitude. That emitted by the blackbody at 1000 °C remains higher, but increases by just a single order of magnitude between the two wavelengths.
- At 12 μm spectral radiant exitance from the blackbody at 0 °C is still less than that for the 1000 °C blackbody, but the difference is now the smallest of the three cases.

By holding wavelength constant we can also use the Planck Function to see how, at a given wavelength, spectral radiant exitance will increase with the temperature of the blackbody. The relationships between spectral radiant exitance and temperature for measurements made in the shortwave infrared, the mid-infrared and thermal infrared are given in Figure 2.2. This plot illustrates three other key points:

(1) for a given wavelength, spectral radiant exitance increases with temperature;
(2) the rate of change in spectral radiant exitance with temperature is greater for short wavelengths than for long wavelengths; so that
(3) as temperature increases the wavelength of dominant emission decreases.

From Figure 2.2 we see that, for a blackbody at 0 °C, spectral radiant exitance is greatest at 12 μm and least at 1.1 μm. However, as temperature increases, so the spectral radiant exitance recorded at shorter wavelengths overtakes that recorded at longer wavelengths. As a result, spectral radiant exitance is greater at 12 μm than at 3.5 μm until 200 °C. At this point, the 3.5 μm plot crosses the 12 μm plot, so that spectral radiant exitance at 3.5 μm exceeds that at 12 μm. At 750 °C, maximum spectral radiant exitance shifts to 2.5 μm. If the plot was extended to 1530 °C, then peak emission would be recorded at 1.1 μm. In short, as temperature increases, so the wavelength at which peak spectral radiant exitance is recorded decreases. This is Wein's Displacement Law.

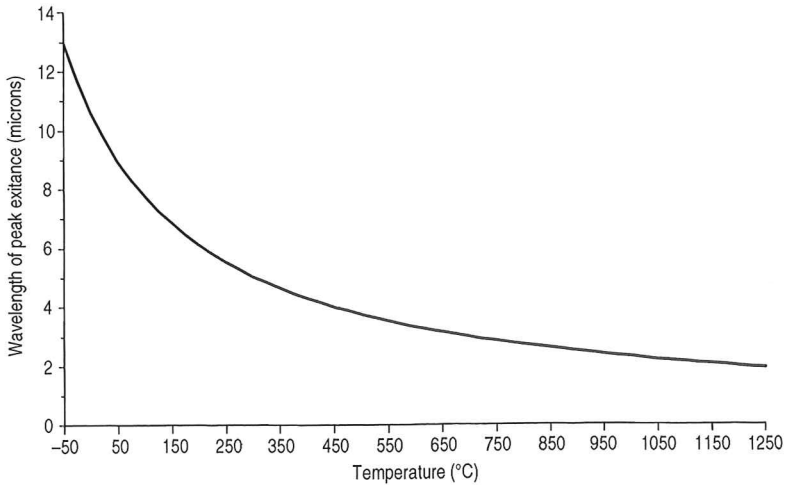


Figure 2.3 Variation in wavelength of peak emission with temperature plotted following Wein's Displacement Law.

### 2.1.1 Wein's Displacement Law

As temperature increases, so the wavelength of peak spectral radiant exitance moves to shorter wavelengths. This behavior is described by Wein's Displacement Law, which relates the wavelength at which the blackbody radiation curve reaches a maximum ($\lambda_m$) to the temperature of the blackbody ($T$, in Kelvin) through:

$$\lambda_m = \frac{A}{T} \quad (\mu m), \tag{2.2}$$

$A$ being Wien's constant (2898 μm K).

The wavelengths of peak spectral radiant exitance for blackbodies radiating at typical ambient and active lava temperatures are plotted in Figure 2.3 and given in Table 2.2. These show the following.

- Peak spectral radiant exitance for Earth ambient surfaces is recorded in the thermal infrared.
- For crusted lava surfaces at between 250 °C and 800 °C, the wavelength of peak spectral radiant exitance shifts towards the mid-infrared.
- For bodies at magmatic temperatures (1000 °C to 1200 °C), peak spectral radiant exitance is recorded in the shortwave infrared.

Hence, measurements of these three thermal surface types suit measurements in the thermal, mid- and shortwave infrared, respectively.

### 2.1.2 Stefan–Boltzmann

If we integrate the spectral radiant exitance from a blackbody over all wavelengths we obtain radiant flux density ($M_{rad}$):

$$M_{\text{rad}} = \int_0^{\infty} M(\lambda, T)\mathrm{d}\lambda = \int 2\pi hc^2\lambda^{-5}\left(\exp^{\frac{hc}{\lambda kT}} - 1\right)^{-1}\mathrm{d}\lambda = \frac{2\pi^5 k^4 T^4}{15c^2h^3} \quad (\mathrm{W\ m^{-2}})$$

so that $M_{\text{rad}}$ can be written,

$$M_{\text{rad}} = \frac{2\pi^5 k^4}{15c^2h^3}T^4. \tag{2.3a}$$

This allows us to isolate and combine constants $k$, $c$ and $h$, so that,

$$\frac{2\pi^5 k^4}{15c^2h^3} = \frac{(2)(3.14)^5(1.38\times10^{-23}\mathrm{JK^{-1}})^4}{(15)(6.6256\times10^{-34}\mathrm{Js})^2(2.9979\times10^{8}\mathrm{m\ s^{-1}})^3} = 5.67\times10^{-8}\ \mathrm{Wm^{-2}K^{-4}}.$$

This is the Stefan–Boltzmann constant ($\sigma$), which allows us to reduce Equation (2.3a) to:

$$M_{\text{rad}} = \sigma T^4\ (\mathrm{W\ m^{-2}}). \tag{2.3b}$$

This relation defines the radiated heat flux density from a blackbody, i.e., heat flux per unit area, and shows that spectral radiant exitance from a blackbody increases with temperature following a power-law relationship. The $T^4$ dependency of $M_{\text{rad}}$ means that spectral radiant exitance from a blackbody at 1000 °C is three orders of magnitude higher than that from a blackbody at 0 °C, $M_{\text{rad}}$ being $2\times10^5$ W m$^{-2}$ and $3\times10^2$ W m$^{-2}$ respectively.

Multiplying Equation (2.3b) by the surface area ($A_{\text{surf}}$) of the body emitting at temperature $T$ now gives the radiant flux, i.e.,

$$M_{\text{rad}}\,A_{\text{surf}} = \Phi_{\text{rad}}\quad (\mathrm{W\ or\ J\ s^{-1}}). \tag{2.3c}$$

Finally, integrating through time ($t$) gives radiant energy, i.e.,

$$\Phi_{\text{rad}}t\ =\ Q_{\text{rad}}\ (\mathrm{J}). \tag{2.3d}$$

### 2.1.3 *Lambertian radiation and the steradian*

Radiation from a blackbody is Lambertian or diffuse. That is, there is little or no directional character to the emission so that radiation is distributed uniformly over the entire hemisphere above the surface. As a result, radiance from the Lambertian surface is equal in all directions, as sketched in Figure 2.4. Given such emission properties, spectral radiant exitance from a point source will be projected onto the surface of the hemisphere over an area defined by the solid (three-dimensional) angle ($\mathrm{d}\Omega$). This is the steradian (sr), which is otherwise defined as the "angle formed when the area ($A$) delimited on the surface of a sphere is equal to the square of the radius ($r$) of the sphere" (Mather, p.6, 1987). As shown in Figure 2.5, this means that the angle defining the steradian ($\mathrm{d}\Omega$) is equal to $A/r^2$. As a result, the steradian is

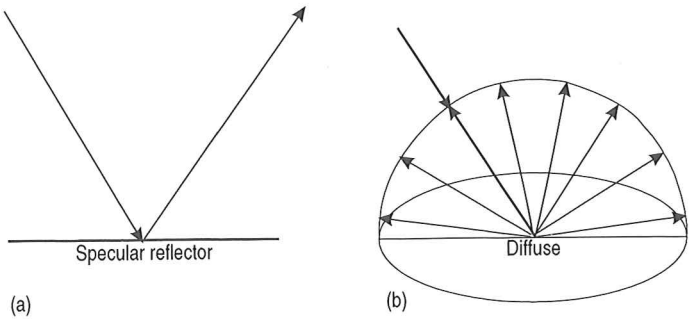


Figure 2.4 Reflectance characteristics of idealized surfaces: (a) a specular reflector and (b) a diffuse reflector [from Schott (2007 Fig. 4.7), by permission of Oxford University Press, Inc].

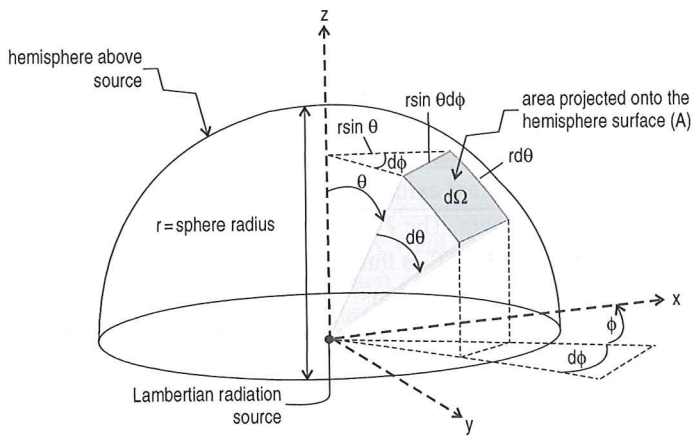


Figure 2.5 Schematic showing the projection of radiation from a point source onto the surface of a hemisphere above that point, illustrating the concept of the solid angle [from Schott (2007, Fig. 3.14) by permission of Oxford University Press, Inc].

dimensionless, being $m^2/m^2$.Thus, as defined in Figure 2.5, spectral radiance measured by the sensor (in W $sr^{-1}$ $m^{-2}$) can be defined as the proportion of the radiant exitance (in W $m^{-2}$) from a blackbody that would be measured at the edge of the hemisphere. The geometry for Lambertian blackbody radiant exitance means that the relationship between spectral radiance $[L(\lambda,T)]$ and radiant exitance $[M(\lambda,T)]$ is

$$L(\lambda, T) = M(\lambda, T)/\pi. \tag{2.4a}$$

Thus, $M(\lambda,T)$ obtained from the Planck Function can be expressed in terms of spectral radiance, $L(\lambda,T)$, following:

$$L(\lambda, T) = \frac{M(\lambda, T)}{\pi} = 2hc^2\lambda^{-5}\left[\exp^{\frac{hc}{\lambda kT}} - 1\right]^{-1} \quad \left(\text{W sr}^{-1}\ \text{m}^{-2}\ \text{m}^{-1}\right), \tag{2.4b}$$

which can be simplified to

$$L(\lambda, T) = \frac{M(\lambda, T)}{\pi} = c_3 \lambda^{-5} \left[ \exp^{\frac{c_2}{\lambda T}} - 1 \right]^{-1} \quad \left( \mathrm{W\ sr^{-1}\ m^{-2}\ m^{-1}} \right) \tag{2.4c}$$

in which

$$c_3 = 2hc^2 = 1.19 \times 10^{-16}\ \mathrm{W\ sr^{-1}\ m^{-2}},$$

this being constant $c_1$ of Equation (2.1b) divided by $\pi$.

### 2.1.4 Temperature and radiance conversion

The Planck Function allows us to convert spectral exitance from a blackbody at wavelength $\lambda$ to the temperature ($T$) of that blackbody. Because the units in Equation (2.1) are in meters, wavelengths must be input into Equation (2.1) in units of meters, so that (for example) 3 μm will be $3 \times 10^{-6}$ m. Now, for a temperature of 290 K, inputting a wavelength of $3 \times 10^{-6}$ m into Equation (2.1b) gives a spectral radiant exitance of

$$M(\lambda, T) = \frac{(3.741 \times 10^{-16}\ \mathrm{Wm^{-2}})}{(3 \times 10^{-6}\ \mathrm{m})^5} \left( \exp^{\frac{(1.4393 \times 10^{-3}\ \mathrm{mK})}{(3 \times 10^{-6}\ \mathrm{m})(290\ \mathrm{K})}} - 1 \right)^{-1} = 1.01 \times 10^5\ \mathrm{W\,m^{-2}\,m^{-1}}.$$

This converts to a spectral radiance of

$$L(\lambda, T) = \frac{M(\lambda, T)}{\pi} = \frac{(1.01 \times 10^5\ \mathrm{Wm^{-2}m^{-1}})}{(3.14)} = 3.20 \times 10^4\ \mathrm{W\ sr^{-1}\,m^{-2}\,m^{-1}}.$$

Dividing by $10^6$ gives wavelength in units of μm. That is,

$$\frac{(3.20 \times 10^4\ \mathrm{W\ sr^{-1}\ m^{-2}\ m^{-1}})}{10^6} = 3.20 \times 10^{-2}\ \mathrm{W\ sr^{-1}\ m^{-2}\ \mu m^{-1}}.$$

Inversion of the Planck Function now allows spectral exitance to be converted back to temperature:

$$T = \frac{c_2}{\lambda \ln\left( \frac{c_1 \lambda^{-5}}{M(\lambda, T)} + 1 \right)}. \tag{2.5}$$

In solving these equations, all we have to do is to check that the input units are correct. For example, constants $c_1$ and $c_2$ used in Equation (2.5) are $3.741 \times 10^{-16}$ W m$^{-2}$ and $1.4393 \times 10^{-2}$ m K. Thus, temperature and $M(\lambda,T)$ must be entered in units consistent with the constants' units, i.e., temperature must be input in Kelvin (= centigrade plus 273.15) and $M(\lambda,T)$ in W m$^{-2}$ m$^{-1}$. If, instead, spectral radiance is input in units of W sr$^{-1}$ m$^{-2}$ m$^{-1}$, then either $L(\lambda,T)$ must first be divided by $\pi$, so as to convert to units of W m$^{-2}$ m$^{-1}$, or $c_1$ must be replaced by $c_3$. Likewise, if $M(\lambda,T)$ is in wavelength units of per micron (W m$^{-2}$ μm$^{-1}$), then $M(\lambda,T)$ must be multiplied by $10^6$ to convert to W m$^{-2}$ m$^{-1}$.

### 2.1.4.1 Worked example

For the AVHRR, sensor spectral radiances are recorded in units of milliwatts/m$^2$-steradian-cm$^{-1}$ (Kidwell, 1991). In this case, wavelength will have to be entered into the Planck Function as a wavenumber in cm$^{-1}$. Constant $c_3$ will be $1.191 \times 10^{-5}$ mW sr$^{-1}$ cm$^{-4}$ (so that $c_1 = c_3/\pi = 3.791 \times 10^{-6}$ mW cm$^{-4}$), and $c_2$ will be 1.439 cm K. The Planck Function for spectral radiance also needs to be modified to

$$L(v,T) = c_3 v^3 \left[\exp^{\frac{c_2 v}{T}} - 1\right]^{-1} \qquad (\text{mW sr}^{-1}\,\text{m}^{-2}\,\text{cm}^{-1}), \tag{2.6a}$$

$v$ being wavenumber (in cm$^{-1}$). Thus, three microns becomes 1/0.0003 cm or 3333 cm$^{-1}$. Now, for a temperature of 290 K, we obtain a spectral radiance of

$$\begin{aligned} L(\lambda,T) &= (1.191 \times 10^{-5}\ \text{mW sr}^{-1}\ \text{cm}^{-4})\,(3333\ \text{cm}^{-1})^3 \left(\exp^{\frac{(1.439\ \text{cm K})(3333\ \text{cm}^{-1})}{(290\ \text{K})}} - 1\right)^{-1} \\ &= 0.0289\ \text{mW sr}^{-1}\ \text{m}^{-2}\ \text{cm}^{-1}, \end{aligned}$$

which converts to a spectral radiant exitance of

$$M(1,T) = \pi L(\lambda,T) = (3.14)\left(0.0289\ \text{mW sr}^{-1}\ \text{m}^{-2}\ \text{cm}^{-1}\right) = 0.091\ \text{mW m}^{-2}\ \text{cm}^{-1}.$$

Inversion of Equation (2.6a) allows conversion of spectral radiance back to temperature, that is,

$$T = \frac{c_2 v}{\ln\left(1 + \frac{c_3 v^3}{L(v,T)}\right)} \quad (\text{kelvin}), \tag{2.6b}$$

so that

$$T = \frac{(1.439\ \text{cm K})(3333\ \text{cm}^{-1})}{\ln\left(1 + \frac{(1.191 \times 10^{-5}\text{mW sr}^{-1}\ \text{cm}^{-4})(3333\ \text{cm}^{-1})^3}{(0.0289\ \text{mW sr}^{-1}\text{m}^{-2}\text{cm}^{-1})}\right)} = 290\ \text{K}.$$

These relationships are essential in converting pixel radiances to temperature, and temperature back to radiance. They thus underpin many of the mathematical operations applied in processing and applying thermal data acquired over active volcanic targets.

## 2.2 Emissivity

So far we have assumed blackbody behavior. This assumption means that the surface is considered to be an ideal radiator which totally absorbs and then reemits all energy incident upon it. In such cases reflectivity is zero and absorptivity is one.

In reality, most surfaces do not display blackbody behavior and instead emit only a fraction of the energy emitted from a blackbody. The emitting ability of such a non-blackbody surface is described by emissivity, $\varepsilon(\lambda)$. This will vary with wavelength and viewing angle. Emissivity can thus be defined as the ratio of spectral exitance, $M(\lambda,T)$, from

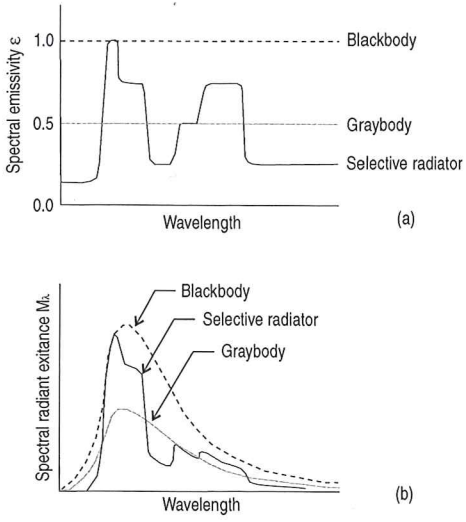


Figure 2.6 (a) Variation in emissivity with wavelength for a blackbody, graybody and selective radiator, and (b) the effect that each of these spectral emissivity curves have on the spectral radiant exitance from a blackbody, graybody and selective radiator [from Lillesand and Kiefer (1987, Fig. 7.3). This material is reproduced with permission of John Wiley & Sons, Inc.].

an object at wavelength $\lambda$ and temperature $T$, to that from a blackbody at the same wavelength and temperature, $M_{BB}(\lambda,T)$:

$$\varepsilon(\lambda) = \frac{M(\lambda, T)}{M_{BB}(\lambda, T)}. \tag{2.7}$$

A graybody has an emissivity of less than 1, i.e., $M(\lambda,T) < M_{BB}(\lambda,T)$. For a graybody, emissivity is also constant at all wavelengths, so that at any given wavelength the spectral exitance from the graybody is a constant fraction of that from the blackbody at the same temperature. If emissivity varies with wavelength, then the body is a selective radiator. In this case the spectral exitance from the graybody is a variable fraction of that from the blackbody at the same temperature, with the fraction varying with wavelength as shown in Figure 2.6a.

### 2.2.1 *The Kirchoff Radiation Law*

All energy incident upon a body ($E_I$) must either be absorbed by it ($E_A$), reflected from it ($E_R$), or transmitted through it ($E_T$) so that:

$$E_I = E_A + E_R + E_T. \tag{2.8a}$$

If we assume that no radiation is transmitted through the body (i.e., the body is opaque to thermal radiation), then $E_T = 0$ and Equation (2.8a) reduces to:

$$E_I = E_A + E_R. \tag{2.8b}$$

Dividing by $E_I$ allows the equation to be expressed as a ratio of the energy incident upon the surface of the body to that either absorbed or reflected by it:

$$\frac{E_I}{E_I} = \frac{E_A}{E_I} + \frac{E_R}{E_I}. \tag{2.8c}$$

The right-hand terms now comprise ratios that can be used to describe the absorptance, $\alpha(\lambda)$, and reflectance, $\rho(\lambda)$, of the body:

$$\alpha(\lambda) = \frac{E_A}{E_I} \tag{2.8d}$$

$$\rho(\lambda) = \frac{E_R}{E_I} \tag{2.8e}$$

so that Equation (2.8c) can also be written:

$$\alpha(\lambda) + \rho(\lambda) = 1. \tag{2.8f}$$

In other words, all energy available to the body is either absorbed into it, or reflected by it. In the case of a blackbody, $\rho(\lambda) = 0$, so $\alpha(\lambda)$ must be 1. Kirchoff's Radiation Law states that the spectral emissivity of a body equals its spectral absorptance, i.e., $\varepsilon(\lambda) = \alpha(\lambda)$. Thus, replacing $\alpha(\lambda)$ with $\varepsilon(\lambda)$ in Equation (2.8f) results in:

$$\varepsilon(\lambda) + \rho(\lambda) = 1. \tag{2.8g}$$

Thus, we have a direct relationship whereby, in the thermal infrared region of the spectrum:

$$\varepsilon(\lambda) = 1 - \rho(\lambda). \tag{2.8h}$$

That is, the higher the spectral reflectance of a surface, the lower the emissivity. This now allows emissivity to be calculated from spectral reflectance measurements. Simply, we place the measurement for $\rho(\lambda)$ into Equation (2.8h) and we have $\varepsilon(\lambda)$. Spectral reflectance (measured across the 8–14 μm waveband) and the $\varepsilon(\lambda)$ that these yield are given, for a range of volcanic surface types, in Table 2.3.

### 2.2.2 Emissivity, radiation and kinetic temperature

The Planck Function, as given in Equation (2.1), applies to a blackbody radiator and yields spectral radiant exitance for a blackbody, $M_{BB}(\lambda,T)$. We can estimate spectral radiant exitance from a non-blackbody, $M(\lambda,T)$, by reducing $M_{BB}(\lambda,T)$ by the spectral emissivity of the body, that is:

$$M(\lambda, T) = \varepsilon(\lambda) M_{BB}(\lambda, T) = \varepsilon(\lambda) 2\pi h c^2 \lambda^{-5} \left[\exp^{\frac{hc}{\lambda k T}} - 1\right]^{-1}, \tag{2.9}$$

Table 2.3. *Broad-band (8–14 μm) spectral reflectance [$\rho(\lambda)$], and the emissivity [$\varepsilon(\lambda)$] that this yields, for the range of volcanic surfaces for which the spectral emissivity are plotted in Figure 2.7. First, the blackbody spectral exitance, $M_{BB}(\lambda,T)$, is given for a range of kinematic temperatures ($T_{kin}$) typical of each active volcanic surface. Next, the actual spectral exitance for each non-blackbody source, $M(\lambda,T)$, is given. This is obtained by multiplying the spectral exitance expected from a blackbody at temperature $T$ (= $T_{kin}$) by the emissivity of that body [i.e., $M(\lambda,T) = \varepsilon(\lambda)\, M_{BB}(\lambda,T)$]. Finally, the radiative temperature ($T_{rad}$) that each $M(\lambda,T)$ yields is given. The radiative temperature is, for all non-blackbody cases where $\varepsilon(\lambda) < 1$, always less then the kinematic temperature (i.e., $T_{kin} - T_{rad}$ is negative). This a result is the object being an imperfect emitter.*

| Body | $\rho(\lambda)$ 8–14 μm | $\varepsilon(\lambda)$ 8–14 μm | $T_{kin}$, K (°C) | $M_{BB}(\lambda,T)$ (W $m^{-2}$ $m^{-1}$) | $M(\lambda,T)$ (W $m^{-2}$ $m^{-1}$) | $T_{rad}$, K (°C) | $T_{kin} - T_{rad}$ K or °C |
|---|---|---|---|---|---|---|---|
| BLOCK 1: Basalt at constant temperature (1000 °C) and increasing emissivity | | | | | | | |
| Basalt: Kilauea, glassy pahoehoe (2 months old) | 0.1 | 0.9 | 1273 (1000) | 1.29E+09 | 1.16E+09 | 1193 (920) | −80 |
| Basalt: Kilauea, ropey pahoehoe (2 months old) | 0.057 | 0.943 | 1273 (1000) | 1.29E+09 | 1.22E+09 | 1228 (955) | −45 |
| Basalt: Kilauea, 'A'a (26 years old) | 0.046 | 0.954 | 1273 (1000) | 1.29E+09 | 1.23E+09 | 1236 (963) | −37 |
| Basalt: Etna slabby (spiney) pahoehoe (2 months old) | 0.043 | 0.957 | 1273 (1000) | 1.29E+09 | 1.24E+09 | 1239 (966) | −34 |
| Basalt: Etna 'A'a (3 years old) | 0.029 | 0.971 | 1273 (1000) | 1.29E+09 | 1.26E+09 | 1250 (977) | −23 |
| Blackbody at 1000 °C | 0 | 1 | 1273 (1000) | 1.29E+09 | 1.29E+09 | 1273 (1000) | 0 |
| BLOCK 2: Sulfur at constant temperature (100 °C) and increasing emissivity | | | | | | | |
| Fresh sulfur surface: Vulcano | 0.14 | 0.86 | 373 (100) | 7.18E+07 | 6.18E+07 | 358 (85) | −15 |
| Weathered sulfur surface: Vulcano | 0.091 | 0.909 | 373 (100) | 7.18E+07 | 6.53E+07 | 364 (90) | −10 |
| Blackbody at 100 °C | 0 | 1 | 373 (100) | 7.18E+07 | 7.18E+07 | 373 (100) | 0 |
| BLOCK 3: Trachytic-rhyolitic lava at decreasing temperature and constant emissivity (0.975) | | | | | | | |
| Trachytic-rhyolitic: Vulcano (erupted in 1888–90) | 0.025 | 0.975 | 1273 (1000) | 1.29E+09 | 1.26E+09 | 1253 (980) | −20 |
| Trachytic-rhyolitic: Vulcano (erupted in 1888–90) | 0.025 | 0.975 | 1023 (750) | 8.96E+08 | 8.74E+08 | 1009 (736) | −14 |
| Trachytic-rhyolitic: Vulcano (erupted in 1888–90) | 0.025 | 0.975 | 773 (500) | 5.24E+08 | 5.11E+08 | 764 (491) | −9 |
| Trachytic-rhyolitic: Vulcano (erupted in 1888–90) | 0.025 | 0.975 | 523 (250) | 2.07E+08 | 2.02E+08 | 518 (245) | −5 |
| Trachytic-rhyolitic: Vulcano (erupted in 1888–90) | 0.025 | 0.975 | 373 (100) | 7.18E+07 | 7.00E+07 | 371 (97) | −3 |

$M_{BB}(\lambda,T)$ being the radiant exitance for a blackbody at temperature $T$ and wavelength $\lambda$. The emissivity effect on the Planck curve for spectral radiant exitance for a graybody and a selective radiator is shown graphically in Figure 2.6b.

The radiant flux density from a non-blackbody source also needs to be reduced by the emissivity factor, so that the Stefan–Boltzmann relation needs to be written:

$$M_{rad} = \varepsilon\sigma T^4 \quad \left(\mathrm{W\ m^{-2}}\right). \tag{2.10}$$

In this case ε is emissivity integrated over all wavelengths.

A thermal sensor will record the radiation temperature ($T_{rad}$) of a surface, without taking into account emissivity effects, that is:

$$T_{rad} = \frac{c_2}{\lambda \ln\left(\frac{c_1\lambda^{-5}}{M(\lambda,T)} + 1\right)}. \tag{2.11a}$$

Because emissivity has not been taken into account, this will provide an underestimate of the true, kinetic, temperature of the surface if emissivity is less than one. To obtain kinetic temperature ($T_{kin}$), the emissivity of that surface must be accounted for, i.e.,

$$T_{kin} = \frac{c_2}{\lambda \ln\left(\frac{\varepsilon(\lambda)c_1\lambda^{-5}}{M(\lambda,T)} + 1\right)}. \tag{2.11b}$$

Thus, for non-blackbody sources, we need to divide the spectral exitance recorded by the sensor [M(λ,T)] by emissivity to obtain the blackbody-equivalent spectral exitance or kinetic temperature:

$$M(\lambda,T)/\varepsilon(\lambda) = M_{BB}(\lambda,T) = 2\pi hc^2\lambda^{-5}\left[\exp^{\frac{hc}{\lambda kT}} - 1\right]^{-1}. \tag{2.11c}$$

The expected difference between the kinetic and radiation temperature for a number of volcanic surfaces is given in Table 2.3. Note that $T_{kin}$ is only equal to $T_{rad}$ for a blackbody where $\varepsilon(\lambda) = 1$. From Table 2.3 we see that emissivities in the 8–14 μm waveband for active volcanic surfaces are always less than 1, so that none of the Table 2.3 surfaces are blackbodies. Table 2.3 shows that, by making the assumption that the surface is a blackbody emitter (and thus not correcting for emissivity) will result in an error (underestimate) in the assessment of true surface (kinematic) temperature by 10 to 80 °C. This underestimate is revealed by the difference between the body's kinematic and radiative temperature calculated for the 8–14 μm waveband, as given in the final column of Table 2.3. As can be seen from the first block of basaltic surface types given in Table 2.3, for an active lava at 1000 °C, the difference between $T_{kin}$ and $T_{rad}$ decreases as emissivity increases. The same effect is apparent in the second block of Table 2.3 where typical emissivities for sulfur are used to calculate the expected $T_{rad}$ for a sulfur-encrusted fumarole at 100 °C. The final (third) block of Table 2.3 shows, using the emissivity for a trachytic-rhyolitic lava flow, how the difference between $T_{kin}$ and $T_{rad}$ will also decease (for a constant emissivity) with kinematic temperature.

Table 2.4. *Summary statistics for the maximum, minimum and mean emissivities across the 2–15 μm waveband for a range of volcanic surface types, with wavelength location of maximum ($\lambda_{max}$) and minimum ($\lambda_{min}$) emissivity. The reflectance spectra from which these statistics are derived are given in Figure 2.7. All samples were measured between 2.08 μm and 14.98 μm using a Nicolet system FTIR spectrometer by J. Salisbury (Johns Hopkins University) during December 1995.*

| Surface composition, location and type (sample age, at time of measurement, is given in parentheses) | Maximum $\varepsilon$ | $\lambda_{max}$ (μm) | Minimum $\varepsilon$ | $\lambda_{min}$ (μm) | Mean $\varepsilon$ |
|---|---|---|---|---|---|
| Basalt: Kilauea, glassy pahoehoe (2 months old) | 0.995 | 8.2 | 0.822 | 10.2 | 0.91 |
| Basalt: Kilauea, ropey pahoehoe (2 months old) | 0.992 | 8.3 | 0.903 | 10.5 | 0.96 |
| Basalt: Kilauea, 'A'a (26 years old) | 0.993 | 14.9 | 0.904 | 9.1 | 0.95 |
| Basalt: Etna slaby (spiney) pahoehoe (2 months old) | 0.988 | 8.2 | 0.932 | 10.8 | 0.95 |
| Basalt: Etna 'A'a (3 years old) | 0.987 | 8.0 | 0.956 | 10.3 | 0.97 |
| All basalts | 0.995 | 8.2 | 0.956 | 10.3 | 0.95 |
| Trachytic-rhyolitic: Vulcano (erupted in 1888–90) | 0.991 | 6.0 | 0.813 | 2.2 | 0.95 |
| Fresh sulfur surface: Vulcano | 0.924 | 11.8 | 0.450 | 2.2 | 0.74 |
| Weathered sulfur surface: Vulcano | 0.927 | 14.9 | 0.577 | 2.1 | 0.80 |

### 2.2.3 *Emissivity of lavas*

Between 2 μm and 15 μm, emissivity of basalt is generally between 0.9 and 0.99, with a mean of 0.95 (see Table 2.4). Thus, basaltic surfaces are not blackbody sources. From Figure 2.7 we also see that, although there is not much variation in emissivity with wavelength, there is some. Thus basalts are selective radiators, and an appropriate emissivity should be selected depending on wavelength. For comparison with the basalts, the spectral emissivity of trachyte-rhyolite and sulfur (a common surface at fumarole fields) is also given in Figure 2.7. We see that these too are selective radiators.

The main variation in the spectral emissivity of fresh basalt is due to a broad reflectance feature between 8 μm and 12 μm. As found by Crisp *et al.* (1990), this reflectance feature typically has a peak between 10.3 μm and 10.5 μm in basalts. As a result, and as is apparent from Table 2.4, lowest emissivities for basalts are encountered within the 9–11 μm waveband.

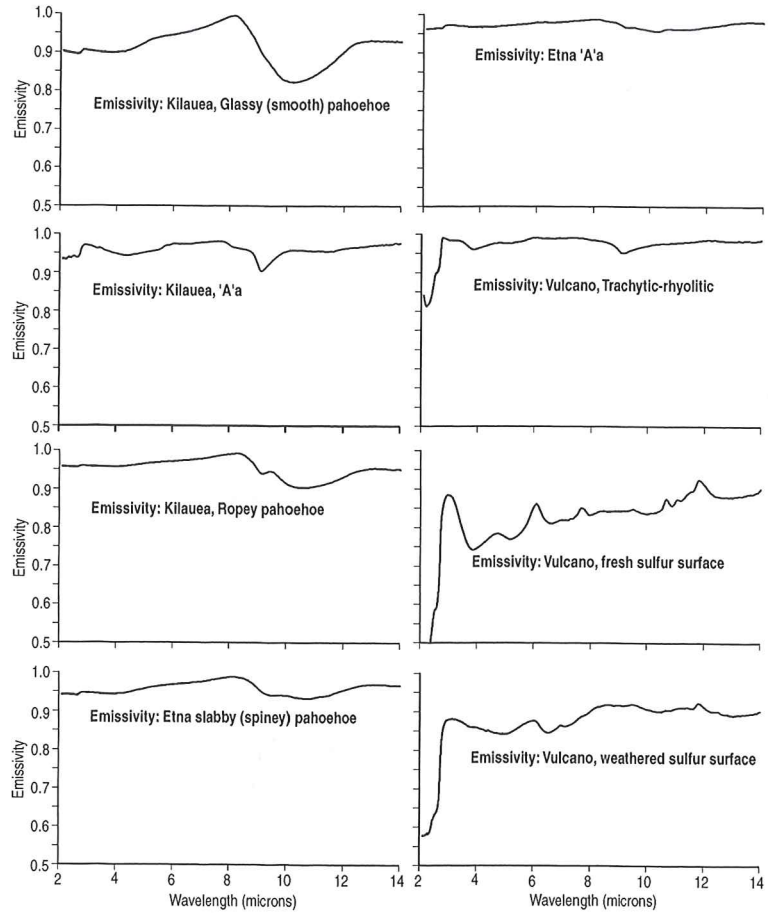


Figure 2.7 Spectral emissivity for a range of common volcanic surface types. Spectral emissivity was calculated from reflectance spectra obtained for samples collected at Kilauea, Etna and Vulcano.

This is due to a strong degree of disorder in volcanic glass, which is made up a variety of silicate units with a variety of bond angles, strengths and arrangements that vibrate at different frequencies (Crisp *et al.*, 1990; Kahle *et al.*, 1995). With time, the unstable configuration breaks down as the silica tetrahedra become organized into sheet-like and chain-like units. This causes the 8–12 μm feature to decay, and the spectra to flatten, with time (Kahle *et al.*, 1995). Again, we see this effect in Table 2.4 where the emissivities in the older silicate samples are typically higher than those for younger samples, meaning that reflection is decaying with time.

### *2.2.4 What emissivity to use?*

We are interested in active features, thus the spectra from (and hence emissivity for) fresh, glassy samples, before aging and/or weathering, are of interest to us. However, most

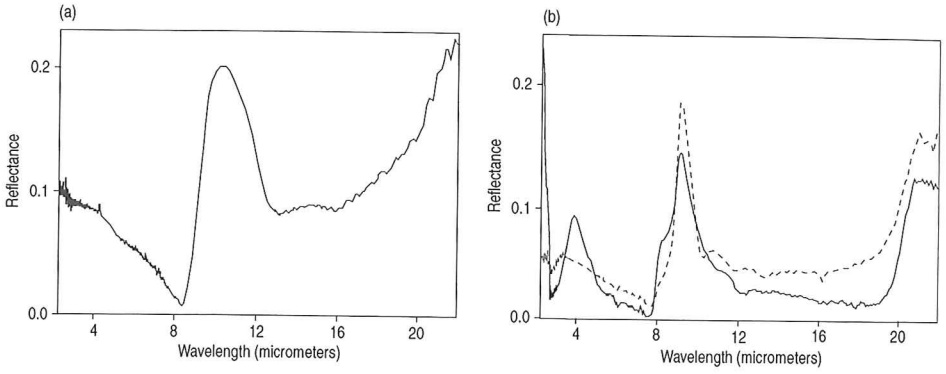


Figure 2.8 (a) Reflectance spectrum for a sample of basalt collected from an active lava flow at Kilauea in May 1989 [from Crisp *et al.* (1990, Fig. 2): reproduced by permission of American Geophysical Union]. (b) Reflectance spectrum for a sample of rhyolite obsidian (solid line) and basalt glass (1984 Mauna Loa basalt collected in May 1989, dashed line) [from Crisp *et al.* (1990, Fig. 15): reproduced by permission of American Geophysical Union].

emissivity measurements to date have been made on solid lava at ambient temperatures, after (at best) a few minutes or (at worst) a few years of emplacement. Measurements on such solid lava samples at ambient temperature indicate that emissivities are high in the 2–15 μm waveband, as shown in Figure 2.7 and summarized in Table 2.4. Reflectance spectra measurements made by Pollack *et al.* (1973), Walter and Salisbury (1989), Crisp *et al.* (1990), Kahle *et al.* (1995), Realmuto *et al.* (1992) and Wells and Cullinane (2007), as well as emissivity values reported by Moxham (1971), are all consistent with the emissivities given in Table 2.4.

Reflectance spectra for Hawaiian lavas, as well as rhyolite obsidian, obtained by Crisp *et al.* (1990), and given here in Figure 2.8, show a strong reflectance feature between 8 μm and 12 μm. This translates to a minimum $\varepsilon(\lambda)$ of ~0.8 for basaltic glass and 0.85 for rhyolite obsidian between 8 μm and 12 μm. Reflectance spectra of Crisp *et al.* (1990) are also consistent with $\varepsilon(\lambda)$ of 0.90–0.95 (for basalt) and ~0.96 (for rhyolite) above 12 μm and below 8 μm. Spectral emissivity obtained by Realmuto *et al.* (1992) for Hawaiian pahoehoe flows of a few months in age are given in Figure 2.9. Like the results of Crisp *et al.* (1990), these give $\varepsilon(\lambda)$ in the 8.5 μm to 11.5 μm waveband of 0.9–0.95. We note also that the increase in emissivity with age, as predicted from the discussion above, can be seen in the spectra-time series given for the Hawaiian (Kilauea) basaltic pahoehoe flow in Figure 2.9, so that the emissivity should also be set depending on the age of the sample. Figure 2.9 shows that an emissivity of ~0.90 may be appropriate at 10.5 μm for basaltic pahoehoe surfaces that are ~5 months old, and ~0.95 for the same surface after two years.

Measurements by Walter and Salisbury (1989) allow consideration of other igneous rock types, as given here in Figure 2.10. These reflectance spectra yield emissivity for andesite of

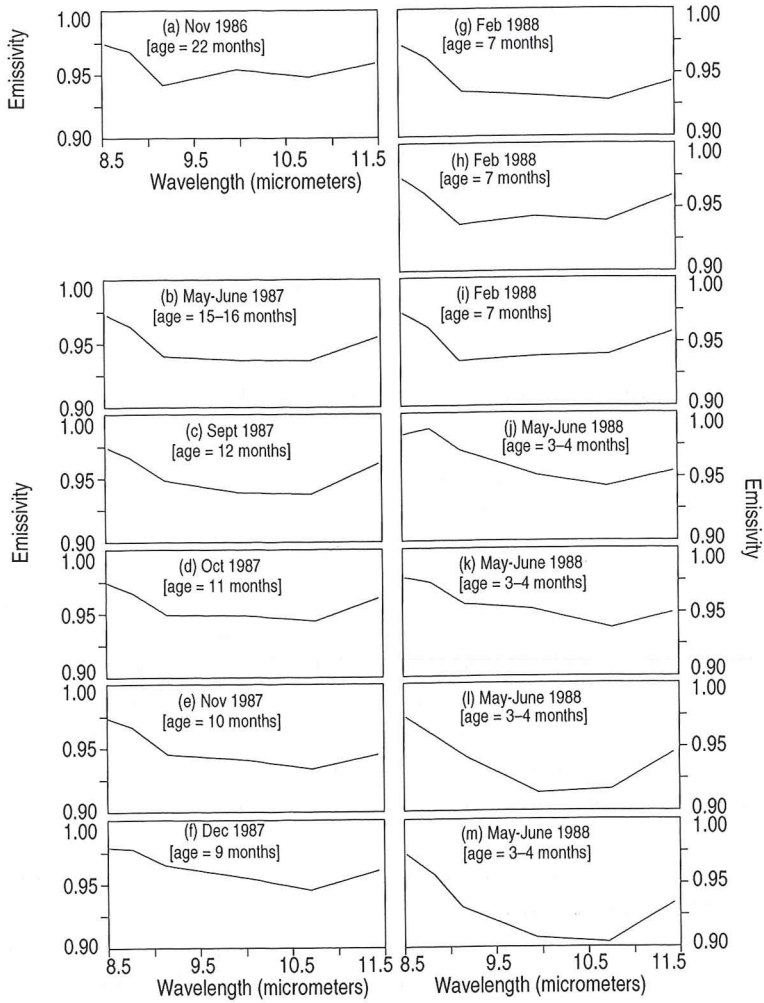


Figure 2.9 Emissivity variation between 8.5 μm and 11.5 μm for basaltic surfaces at Kilauea. Measurement was made on 1 October 1988 using the TIMS sensor, so that the surfaces are between 5 and 48 months old. Spectra decrease in age from the spectra given in (a) through that given in (m), where we see that the emissivity increases with age [from Realmuto *et al.* (1992, Fig. 6): with kind permission from Springer Science and Business Media]. Date given on each graph is that of lava flow emplacement

between 0.91 and 0.95 in the 8–12 μm waveband. For the 8–14 μm waveband, Moxham (1971) provides a nice summary of $\varepsilon(\lambda)$ for different compositions, giving:

- 0.90 for polished basalt,
- 0.95 for rough basalt,
- 0.93–0.95 for olivine basalt,
- 0.91–0.94 for andesite,
- 0.94–0.95 for rhyolite, and
- 0.87–0.90 for rhyolitic obsidian.

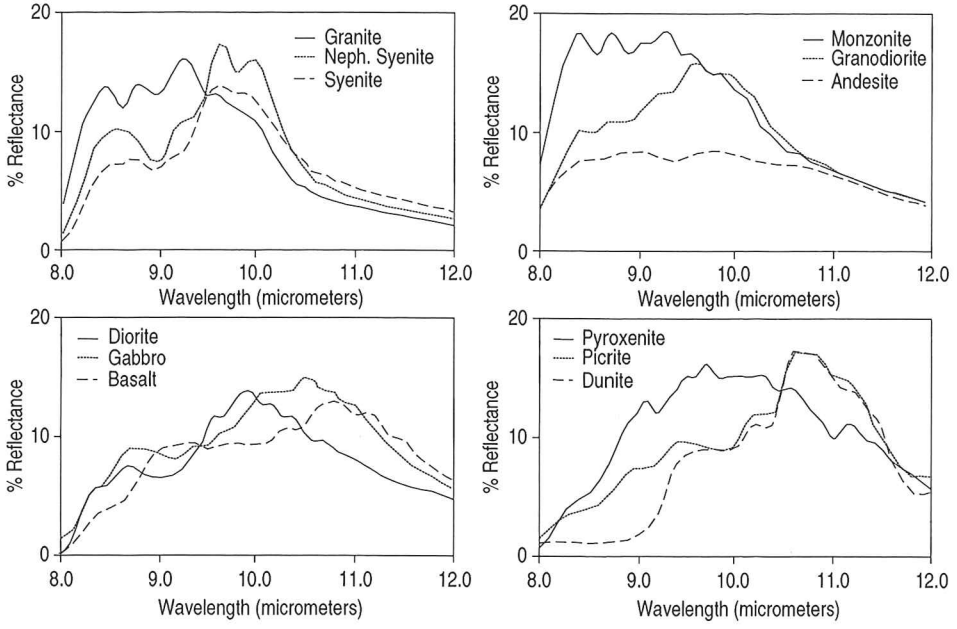


Figure 2.10 Thermal infrared reflectance spectra for a range of igneous rocks [from Walter and Salisbury (1989, Fig. 3): reproduced by permission of American Geophysical Union].

Emissivities for a range of other terrestrial surface types are given (tabulated) in Salisbury and D'Aria (1992), Salisbury and D'Aria (1994) and Salisbury *et al.* (1994).

#### *2.2.4.1 Changes in emissivity between molten and solid lava samples*

There is some evidence that, at short wavelengths, lava reflectance may decrease over the first 24 hours of its lifetime from relatively high values upon emplacement to lower values after a few hours. This means that emissivity will increase from a relatively low value upon emplacement, to higher values for solidified surfaces after a few hours. Using a spectrometer operating in the 1.1–2.5 μm waveband at pahoehoe lava active on Kilauea, we collected reflectance spectra during emplacement of an active lava. These revealed relatively high reflectances of ~25 %, giving an emissivity of ~0.75 (L. Flynn, unpublished data). Reflectance, however, decreased to more typical values with time and cooling, reflectance being less than 10% (giving an emissivity of greater than 0.9) within 24 hours. The high starting reflectance was, however, not always encountered. This means that, in some cases, spectral emissivity between 1.1 μm and 2.5 μm may increase from a low level upon emplacement to levels more typical of those given in Figure 2.7 after a few hours. This may result from highly reflective and coherent glass rinds developing on fresh lava. The presence of such surfaces has been observed to cause reflectance anomalies over fresh pahoehoe flows in satellite (ETM+) data obtained in the 0.52–0.9 μm waveband by Flynn *et al.* (2001). A subsequent decrease in reflectance would result from spalling of this glassy

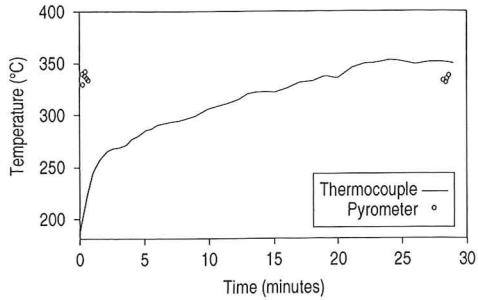


Figure 2.11 Thermocouple-derived temperatures for the surface of Erta Ale's active lava lake as a function of time. Open circles represent the infrared measurements made at the beginning of the experiment and after thermal equilibrium of the thermocouple [from Burgi *et al.* (2002, Fig. 4): with kind permission from Springer Science and Business Media].

rind, to expose an underlying, rougher, vesicular surface, where shedding of the glassy rind during, or shortly after, emplacement is a commonly observed phenomenon on Hawaiian pahoehoe.

By comparing $T_{rad}$ obtained using an optical pyrometer with $T_{kin}$ obtained from a thermocouple in contact with active lava surfaces at the Erta Ale lava lake (Ethiopia), Burgi *et al.* (2002) also obtained low emissivities of 0.74 for a crusted, but active, lava surface (at 350 °C) in the 1.1–1.7 μm waveband. The results of their experiment are given in Figure 2.11. The method applied by Burgi *et al.* (2002) allows emissivity to be calculated from the difference between the kinematic and radiation temperatures obtained for the active lava surface from:

$$\log \varepsilon(\lambda) = \log(\varepsilon_a) + \frac{hc}{\lambda k}\left(\frac{1}{T_{kin}} - \frac{1}{T_{rad}}\right). \tag{2.12a}$$

Here, $\varepsilon_a$ is the arbitrary emissivity used when making the measurement of $T_{rad}$ with the pyrometer, in the case of Burgi *et al.* (2002) the instrument was set to an emissivity ($\varepsilon_a$) of 0.9. This, essentially, is the same as the approach suggested by Brivio *et al.* (1989), whereby the difference between the kinematic and radiation temperatures are used to obtain emissivity in:

$$\varepsilon(\lambda, T) = \frac{\exp(c_2/\lambda T_{kin}) - 1}{\exp(c_2/\lambda T_{rad}) - 1}. \tag{2.12b}$$

Given the $T_{kin}$ of 350 °C and $T_{rad}$ of 342 °C, as measured at Erta Ale's lava lake surface by Burgi *et al.* (2002), and using the mid-point wavelength of their pyrometer (1.4 μm), Equation (2.12a) yields:

$$\log\varepsilon(\lambda) = \log(0.9) + \frac{(6.6256 \times 10^{-34}\ \text{J s})(2.9979 \times 10^{8}\ \text{m s}^{-1})}{(1.4 \times 10^{-6}\text{m})(1.38 \times 10^{-23}\ \text{J K}^{-1})}\left(\frac{1}{(623\ \text{K})} - \frac{1}{(615\ \text{K})}\right)$$

$$= \log(-2.606) = 0.77.$$

Application of the Equation (2.12b) approach gives a slightly higher value:

$$\varepsilon(\lambda, T) = \frac{\exp^{(0.014\ 393\ \text{mK})/[(1.4 \times 10^{-6}\text{m})(623\ \text{K})]} - 1}{\exp^{(0.014\ 393\ \text{mK})/[(1.4 \times 10^{-6}\text{m})(615\ \text{K})]} - 1} = 0.81.$$

Such low emissivities are also consistent with Le Guern *et al.* (1979), who cited a value of 0.7 as being appropriate for basalt in the 9.1–11.2 μm waveband. These measurements thus indicate that, under certain conditions and at certain wavelengths, emissivities of ~0.8 may be appropriate for active (basaltic) lava surfaces.

However, laboratory-based comparisons between radiometer-obtained $T_{rad}$ (in the 0.8–1.1 μm waveband) and thermocouple-obtained $T_{kin}$ for a Hawaiian pahoehoe lava sample by Pinkerton *et al.* (2002) showed best agreement using an emissivity of 1.0 for temperatures between 600 °C and 1000 °C. Likewise, furnace-based measurements on Erta Ale samples by Burgi *et al.* (2002) failed to replicate the low value obtained in the field, with the closest match between the pyrometer- and thermocouple-measured temperatures being obtained using $\varepsilon(\lambda)$ of between 0.87 and 0.89. In addition, application of a low emissivity (0.74) to spectral exitance measurements made at 8–14 μm can yield kinetic temperatures that are unrealistically high. For example, the radiation temperature measured for the surface of the Erta Ale lava lake by Oppenheimer and Yirgu (2002) gave a maximum of 1174 °C which, being obtained using a thermal camera operating in the 8–14 μm waveband, is a radiative temperature. Converting this to radiant exitance using Equation (2.1), correcting for an emissivity of 0.74 and then converting back to kinetic temperature using Equation (2.11b), yields a kinetic temperature of 1500 °C. This is somewhat higher than the expected maximum liquidus temperature at Erta Ale of 1125–1225 °C (from Bizouard *et al.*, 1980), and therefore improbable.

As already argued, one explanation for different emissivities between two surfaces of the same type and at the same temperature is variation in surface roughness. Such a suggestion was made by Burgi *et al.* (2002) to explain the low emissivities at Erta Ale, where the presence of a glassy crust may increase the reflectance over a lava characterized by a rough, vesicular surface. Measurements by Ramsey and Fink (1999) show how the emissivity of rhyolite increases with vesicularity at all wavelengths. The measurements, given here in Figure 2.12, show the minimum emissivity (recorded at ~9 μm) increasing from 0.70 for a surface composed of rhyolite glass to 0.89 for a coarsely vesicular surface. Thus, we would expect emissivity for a lava flow with a glassy surface to be lower than that for a lava with a rough, vesicular surface.

The results reviewed here point to the need to obtain an improved understanding of the variation in emissivity with (1) surface type (and roughness), (2) temperature and (3) wavelength. Measurements thus need to be made through the phase change from molten to solid, and as thin, high-reflective glass coatings and/or rough vesicular surfaces develop. Clearly there are conditions under which emissivity at an active, basaltic lava can be quite low (such as at active flows with a glassy crust), but there are also conditions under which emissivities are high (as is typical for rougher surfaces). For now, the difficulty in replicating

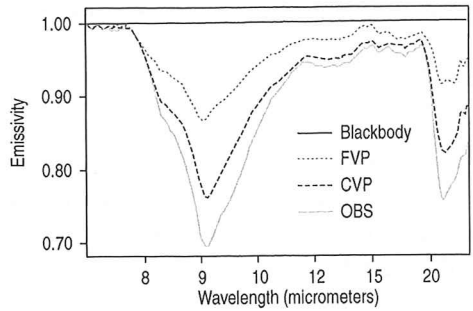


Figure 2.12 Thermal infrared emissivity spectra for a rhyolite glass (OBS), finely vesicular pumice (FVP) and coarsely vesicular pumice (CVP). Spectra are averages of at least ten samples and show how emissivity decreases with increased surface roughness. The absorption band, diagnostic of glass, is observed at 9.25 μm [from Ramsey and Fink (1999, Fig. 1): with kind permission from Springer Science and Business Media].

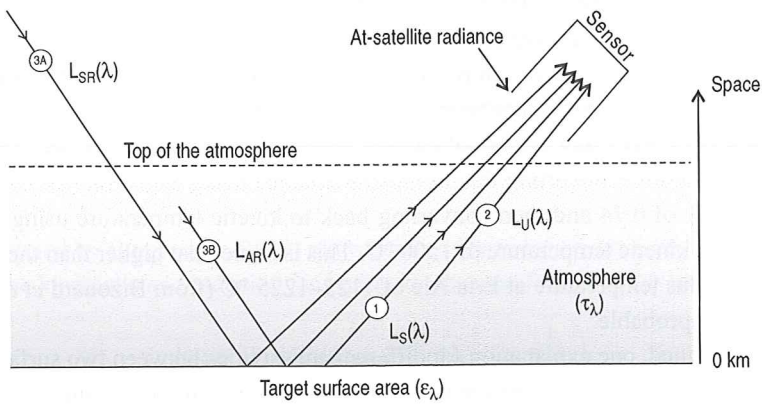


Figure 2.13 Cartoon showing the contributions to satellite-received radiance [based on Cracknell and Hayes (1991, Fig. 8.2)].

our low-reflectance measurements at Kilauea and Erta Ale with commonly measured $\varepsilon(\lambda)$ in the range 0.9–0.99, lead us to suggest that the values of Figure 2.7 are typical. However, emissivity must be selected carefully, and set depending on surface type (and rock composition), temperature, age, roughness, and wavelength of the measurement.

## 2.3 Atmospheric effects

While the atmosphere will both absorb and emit radiation of its own, the surface will also reflect radiation, so that the radiation arriving at the satellite will be an integrated radiance comprising both the surface and atmospheric components, as sketched in Figure 2.13. If this integrated radiance is converted to a temperature using Planck's Formula, it will thus not yield

the surface temperature, but instead a value termed the brightness temperature. Here we deal with the unwanted atmospheric and reflection components, and examine means of obtaining surface temperature from the brightness temperature through atmospheric correction.

**Transmissivity** The atmosphere is not perfectly transparent to infrared radiation. As a result, a portion of the radiance emitted by a surface will be absorbed and back-scattered by the atmosphere. This attenuation effect is described by atmospheric transmissivity, $\tau(\lambda)$. This has a value in the range of one, for a perfectly transparent atmosphere, to zero, for a perfectly opaque atmosphere. Thus, for a surface at temperature $T_s$, surface-leaving radiance, $\varepsilon(\lambda)L(\lambda,T_s)$, will be related to the radiance arriving at the sensor, $L_S(\lambda)$, by:

$$L_S(\lambda) = \tau(\lambda)\, \varepsilon(\lambda)\, L(\lambda, T_s). \tag{2.13a}$$

That is, the radiance emitted by the surface and arriving at the sensor will be reduced by a factor described by the atmospheric transmissivity.

### 2.3.1 Atmospheric windows

As shown in Figure 2.14a, transmissivity varies with wavelength. Hence, the degree of attenuation experienced by surface emitted radiance will vary with wavelength. The resulting effect on the spectral radiant exitance from a blackbody at 1000 °C is illustrated in Figure 2.14b. Across some portions of the spectrum, the atmosphere will absorb most (if not all) of the emitted radiance. However, there are seven atmospheric windows across which emitted radiance suffers less than 10% attenuation (i.e., regions within which $\tau(\lambda)$ is greater than 0.9). As listed in Table 2.5, two of these windows are located in the NIR, three are in the SWIR and one is in the MIR. A broad window also occurs between 8.6 μm and 12.2 μm, i.e., in the TIR. Within these windows, the atmosphere is semi-transparent to emitted radiation. Sensor wavebands for instruments designed to make measurements of emitted radiance by the Earth's surface are thus located within these windows. However, even within these windows, transmissivity is not zero, and ranges from 0.9 at worst, to 0.98 at best (see Table 2.5). Thus, some of the radiance emitted by a surface, will always be attenuated on arrival at the sensor. As a result, some correction will have to made to the at-sensor radiance to take into account this attenuation effect and to allow the surface-leaving radiance to be retrieved.

#### 2.3.1.1 Correction for transmissivity, and variation with altitude and scan angle

Correction for the attenuation effect can be achieved using $\tau(\lambda)$ in:

$$L(\lambda, T_s) = L_S(\lambda) \,/\, \tau(\lambda)\, \varepsilon(\lambda). \tag{2.13b}$$

For a given wavelength, transmissivity will vary with path length, altitude and scan angle. Longer path lengths traverse more atmosphere, so that more of the emitted radiance will be

Table 2.5. *Locations of, and average transmissivities across, the seven main atmospheric windows in the NIR, MIR and TIR. Values obtained using MODTRAN (see Electronic Supplement 4 for a definition and description of the MODTRAN model and its uses for atmospheric correction). MODTRAN was run using a 1976 US Standard atmosphere with a vertical path from sea-level to space (zenith = 180 °, observer height = 100 km), and a $CO_2$ mixing ratio of 380 ppm·v.*

| Window location | Waveband (μm) | Width (μm) | Average $\tau(\lambda)$ | Max $\tau(\lambda)$ | Location of Max $\tau(\lambda)$ (μm) |
|---|---|---|---|---|---|
| NIR | 0.7–0.89 | 0.19 | 0.90 | 0.93 | 0.89 |
| NIR | 1.0–1.1 | 0.1 | 0.94 | 0.95 | 1.07 |
| SWIR | 1.18–1.31 | 0.13 | 0.94 | 0.96 | 1.25 |
| SWIR | 1.51–1.76 | 0.25 | 0.96 | 0.97 | 1.68 |
| SWIR | 2.03–2.36 | 0.33 | 0.96 | 0.98 | 2.14 |
| MIR | 3.44–4.13 | 0.69 | 0.94 | 0.97 | 3.96 |
| TIR | 8.6–12.2 | 3.6 | 0.92 | 0.96 | 10.11 |

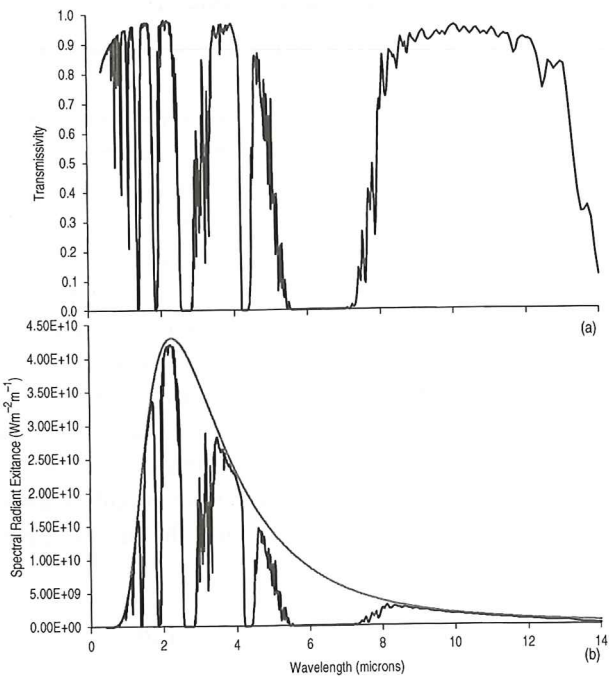


Figure 2.14 (a) Variation in atmospheric transmissivity with wavelength for a MODTRAN US Standard atmosphere (model is run using the same input conditions as used for the simulations of Table 2.5). (b) Effect of atmospheric transmissivity on at-satellite spectral radiance curve for a surface radiating at 1000 °C. See Electronic Supplement 4 for a definition and description of the MODTRAN model and its uses for atmospheric correction.

absorbed as the path length increases, while measurements made at higher altitudes are made in a thinner atmosphere than those at lower altitudes, so that atmospheric attenuation effects decrease with altitude. Path length and altitude effects are significant for ground-based sensors set at variable distances from the source and/or operated at different altitudes, and are considered further in Part III. Here we consider surface altitude and scan angle effects for a satellite-based sensor.

The satellite is at a fixed altitude, typically located several hundred kilometers above the surface. Thus the distance to sea-level remains constant. However, as the satellite passes over terrain of variable elevation, so the path length between the satellite and the surface changes. As elevation of the surface increases, so the path length to the satellite decreases, so that the transmissivity will increase. More importantly, the atmosphere becomes rapidly thinner at higher altitudes, so that attenuation diminishes for satellite observations over surfaces located at higher elevations. For example, 85% of the absorbing gases are found in the lowermost 5 km of the atmosphere (a calculation that excludes $O_2$), with ~90% of atmospheric $H_2O$ being located in this lowermost layer. Thus, although a change in 3 km (the difference in making a measurement at sea-level or Etna's summit) over a surface-to-satellite path length of 800–900 km may not seem like much, the effect of cutting out the lowermost, and least transmissive, layer of the atmosphere is significant. As plotted in Figure 2.15, for a satellite sensor viewing the surface from a vantage point vertically above the surface, transmissivity will increase (i.e., the degree of attenuation will decrease) with surface elevation since the surface at a high elevation has a thinner atmosphere between it and the satellite sensor, so less absorption of the surface-leaving emission occurs.

On the other hand, as the scan angle ($\alpha$) increases (for any given surface elevation), so the atmospheric path length ($L$) will also increase, following $L = \cos(\alpha)/S_h$, $S_h$ being the sensor height above the ground. As a result, to a first approximation (ignoring refraction and scattering), transmissivity will decrease (i.e., the degree of attenuation will increase) with

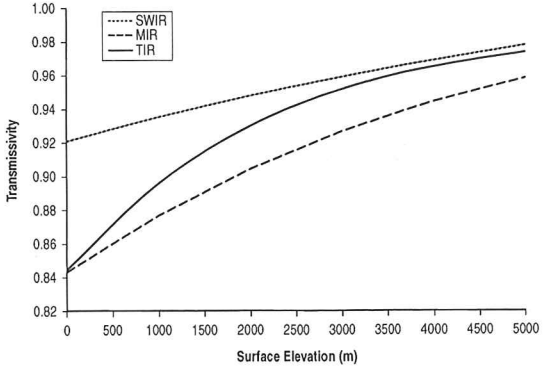


Figure 2.15 Increase in atmospheric transmissivity with surface elevation for a satellite viewing the surface from space in (i) the SWIR (2.1–2.5μm) (ii) the MIR (3.5–4.0 μm) and (iii) the TIR (10–12 μm). The same MODTRAN US Standard atmosphere as used in Figure 2.14 is applied.

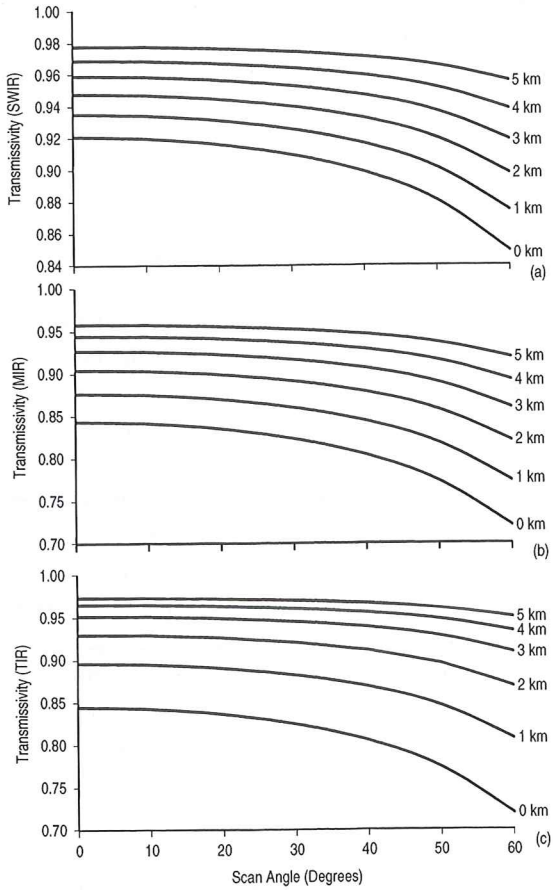


Figure 2.16 Variation in atmospheric transmissivity with scan angle and surface elevation for a satellite viewing the surface from space in (a) the SWIR (2.1–2.5 μm), (b) the MIR (3.5–4.0 μm) and (c) the TIR (10–12 μm). The same MODTRAN US Standard atmosphere as used in Figure 2.14 is applied.

scan angle, as potted in Figure 2.16 since the thickness of the atmosphere through which the surface is viewed increases as the scan angle increases.

### *2.3.2 Atmospheric emission and surface reflection*

As well as attenuating surface-emitted radiance, the atmosphere will also emit radiation. In addition, the surface will reflect radiance. Thus, the at-sensor radiance is actually composed of the radiance emitted from, and reflected by, both the surface and the atmosphere.

Singh and Warren (1983) and Cracknell and Hayes (1991) provide excellent reviews of how the radiance recorded by an infrared sensor is not just the result of surface emission, but

is a complex product of the emission (and attenuation) effects of the intervening atmosphere, as well as the reflective (and hence emissive) properties of the targeted surface. As summarized in Figure 2.13, radiation arriving at the sensor will thus be composed of radiance from three different sources:

(1) radiance emitted by the surface itself, $L_S(\lambda)$,
(2) radiance emitted by (i.e., up-welling from) the atmosphere, $L_U(\lambda)$, and
(3) radiance reflected by the surface, $L_R(\lambda)$.

Hence the make-up of sensor-received radiance, $R_{in}$*, can be written:

$$R^*_{in} = L(\lambda)^* = L_S(\lambda) + L_U(\lambda) + L_R(\lambda). \quad (2.14a)$$

As a result, the temperature value obtained by converting the sensor-arriving radiance to temperature is not the surface temperature ($T_s$), but a brightness temperature ($T^*$). That is,

$$L(\lambda)^* = L(\lambda, T^*) = \varepsilon(\lambda)\,\tau(\lambda)\,L_S(\lambda) + L_U(\lambda) + L_R(\lambda), \quad (2.14b)$$

where $\tau(\lambda)$ needs to be added to describe the attenuating effect of the atmosphere on the surface-leaving radiance. Brightness temperature is thus the sum of radiance from all sources of emitted and reflected radiance that contribute to the sensor-arriving radiance. However, we are interested in the surface temperature. Thus, the quantity that we are interested in is $L_S(\lambda)$, rather than the quantity that we have actually measured, i.e., $L(\lambda)$*. To obtain $L_S(\lambda)$ we must define, constrain and remove the unwanted components, i.e.,

$$L_S(\lambda) = [L(\lambda, T^*) - L_U(\lambda) - L_R(\lambda)] / \varepsilon(\lambda)\,\tau(\lambda). \quad (2.14c)$$

Executing the corrections necessary to eliminate the unwanted quantities, $L_U(\lambda)$ and $L_R(\lambda)$, is not so straightforward, as can be understood by examining the source of each of these quantities.

### 2.3.2.1 Sources of emission

The sensor will be responding to two main sources of emitted radiation. The first is the radiance emitted by the targeted surface, $L_S(\lambda)$. As already shown, this is attenuated as it passes upwards towards the sensor such that, by the time it reaches the sensor, surface-leaving radiance is related to sensor-arriving radiance by $L_S(\lambda) = \tau(\lambda)\varepsilon(\lambda)L(\lambda,T_s)$. The same atmosphere also emits radiation upwards towards the sensor, so that the second source of sensor-arriving radiance is that up-welling from (i.e., emitted towards the sensor by) the atmospheric column, $L_U(\lambda)$.

### 2.3.2.2 Sources of reflection

Surface-reflected radiance has three sources:

(1) solar radiation reflected by the surface towards the sensor, $L_{SR}(\lambda)$,
(2) radiance from space reflected by the surface, $L_{SP}(\lambda)$, and
(3) radiation emitted by the atmosphere that down-wells to the surface to then be reflected back towards the sensor, $L_{AR}(\lambda)$.

Thus surface-reflected radiance arriving at the satellite can be written as

$$L_R(\lambda) = L_{SR}(\lambda) + L_{AR}(\lambda) + L_{SP}(\lambda). \quad (2.15)$$

Of these sources, reflected solar radiation ($L_{\lambda SR}$) will depend on the solar radiance incident upon the Earth's surface, $E_{in}(\lambda)$, and the reflectivity of that surface, $\rho(\lambda)$. $E_{in}(\lambda)$ can be determined from the solar irradiance arriving at the top of the atmosphere (TOA), $\bar{E}_{TOA}(\lambda)$. For the mean Sun–Earth distance this can be estimated from:

$$\bar{E}_{TOA}(\lambda) = M(\lambda, T_{sun})\,(R_S/D_{E\text{-}S})^2, \quad (2.16a)$$

in which $M(\lambda,T_{sun})$ is the radiant exitance from the Sun, $T_{sun}$ is the temperature of the Sun (6000 K), $R_S$ is the radius of the Sun ($695.3 \times 10^6$ m) and $D_{E\text{-}S}$ is the mean Sun–Earth distance ($149.6 \times 10^9$ m). Because the Earth's orbit is elliptic with eccentricity ($e' = 0.0167$), solar radiance arriving at the top of the atmosphere changes slightly from day to day. Actual solar irradiance arriving at the top of the atmosphere, $E_{TOA}(\lambda)$, can thus be obtained from the mean value ($\bar{E}_{TOA}(\lambda)$) using a Julian Day (JD) dependent-correction in Singh and Warren (1983):

$$E_{TOA}(\lambda) = \bar{E}_{TOA}(\lambda)\,\{1 + e' \cos\,[2\pi(JD - 3)/365]\}^2. \quad (2.16b)$$

The incoming solar radiance will be attenuated (absorbed and scattered) by the atmosphere during its downward passage to the surface. The radiance incident upon the surface thus depends on the solar zenith angle ($\theta_S$) and the transmissivity of the atmosphere along the incoming path length [$\tau(\lambda,\theta_S)$], so that

$$E_{in}(\lambda) = \tau(\lambda, \theta_S) \cos(\theta_S)\, E_{TOA}(\lambda). \quad (2.17)$$

The incident solar radiance is then reflected from the surface upwards towards the sensor. As the reflected solar radiation passes upwards through the atmosphere towards the sensor it is again attenuated. Thus, reflected solar radiation arriving at the sensor is described by:

$$L_{SR}(\lambda) = \tau\,(\lambda)\,\rho(\lambda)\,E_{in}(\lambda). \quad (2.18a)$$

Because $\rho(\lambda) = 1 - \varepsilon(\lambda)$, this can also be written

$$L_{SR}(\lambda) = \tau(\lambda)\,[1 - \varepsilon(\lambda)]\,E_{in}(\lambda) \quad (2.18b)$$

or, writing $E_{in}(\lambda)$ in full,

$$L_{SR}(\lambda) = \tau(\lambda)\,[1 - \varepsilon(\lambda)]\,\tau(\lambda, \theta_S) \cos(\theta_S)\, E_{TOA}(\lambda). \quad (2.18c)$$

As detailed in Appendix B, since solar zenith angle (i.e., solar incidence angle) depends on the time of year, time of day, and latitude, so too does $E_{in}(\lambda)$ and, hence also $L_{SR}(\lambda)$.

The second component of surface reflected radiation is reflected atmospheric down-welling radiance. Radiation will be emitted downwards from the atmosphere to the Earth's surface. This, like solar radiation, undergoes reflection upwards towards the sensor. Thus, the amount of down-welling atmospheric radiation, $E_a(\lambda)$, reaching the sensor will depend on the reflectivity of the surface and the transmissivity of the atmosphere through which it passes before arriving at the sensor. That is:

$$L_{AR}(\lambda) = \tau(\lambda)\,\rho(\lambda)\,E_a(\lambda) \quad (2.19a)$$

or, writing $1 - \varepsilon(\lambda)$ for $\rho(\lambda)$,

$$L_{AR}(\lambda) = \tau(\lambda)\,[1 - \varepsilon(\lambda)]\,E_a(\lambda). \quad (2.19b)$$

Following Singh and Warren (1983), a crude estimate of $E_a(\lambda)$ can be obtained from the up-welling radiance, so that replacing $E_a(\lambda)$ with $L_U(\lambda)$ in Equation (2.19b) gives:

$$L_{AR}(\lambda) = \tau(\lambda)\,[1 - \varepsilon(\lambda)]\,L_U(\lambda). \quad (2.19c)$$

The final source of reflected radiation is that from space, $L_{SP}(\lambda)$. Space has a background temperature of ~3 K. This component, $E_{sp}(\lambda)$, passes down through the atmosphere, is reflected by the surface and passes back up through the atmosphere to reach the sensor (Cracknell and Hayes, 1991). Thus, this quantity is given by:

$$L_{SP}(\lambda) = \tau\,(\lambda)\,\rho\,(\lambda)\,\tau_{in}(\lambda)\,E_{sp}(\lambda) \quad (2.20a)$$

or

$$L_{SP}(\lambda) = \tau(\lambda)\,[1 - \varepsilon(\lambda)]\,\tau_{in}(\lambda)\,E_{sp}(\lambda), \quad (2.20b)$$

$\tau_{in}$ being the atmospheric transmissivity experienced by the radiation during its in-coming journey downwards through the atmosphere and $\tau(\lambda)$ being that experienced during its out-going journey upwards to the sensor.

### 2.3.3 Variation of each term between the SWIR, MIR and TIR

The relative contribution of each emission and reflection component to the at-sensor radiance is assessed in Table 2.6a. This considers the atmospheric upwelling and surface reflected contributions to the at-satellite radiance in the SWIR, MIR and TIR from a surface, located at sea-level, to a satellite located vertically overhead. The model is run using a high-emissivity (low-reflection) surface typical of basalt, i.e., $\varepsilon(\lambda)$ is 0.95 at all wavelengths. Two points can be made from the model calculations completed in Table 2.6a.

(1) As we move from the SWIR to the TIR, so the dominant reflected or atmospheric source of emission moves from reflected and back-scattered solar radiation in the SWIR to atmospheric up-welling radiance in the TIR.
(2) By night, with no solar contribution, reflected and scattered solar radiation is zero.

Table 2.6b adds the contribution of an ambient surface radiating at 15 °C to the model. The radiance from such a source in the SWIR is trivial. In fact, the at-sensor radiance is utterly dominated by solar reflected and scattered radiation, so that converting the at-sensor radiance to a brightness temperature is meaningless. By night, the only source in the SWIR is surface emission, but the intensity of the emission is so weak that it would not register a measurable signal at the sensor (see Electronic Supplement 1). Thus, we apply a more realistic (high-temperature) surface emission model for the SWIR in Table 2.6c. This shows that, by day, as we move to a surface temperature of 100 °C the contribution of surface emitted radiance to the total increases to 7%. The contribution of the reflected component, as well as atmospheric attenuation and emissivity effects, result in a brightness

Table 2.6b. *Assessment of total radiance arriving at the sensor, the brightness temperature that this gives, and the contribution of each of the radiance sources to L(λ). Assessment is made for the SWIR (2.1–2.5 μm), MIR (3.5–4.0 μm) and TIR (10–12 μm), during the day and night. The model is run for emission from a surface with an emissivity of 0.95 and at a temperature of 15 °C, with the atmospheric up-welling and surface reflected contributions of Table 2.6a.*

| Day- and night-time emission: surface temperature = 15°C, emissivity = 0.95 | | | | | | | |
|---|---|---|---|---|---|---|---|
| | | Day-time (W $cm^{-2}$ $sr^{-1}$ $\mu m^{-1}$) | | | Night-time (W $cm^{-2}$ $sr^{-1}$ $\mu m^{-1}$) | | |
| Source | Term/derivation | SWIR | MIR | TIR | SWIR | MIR | TIR |
| Surface temperature (°C) | $T_s$ | | 15 °C | | | 15 °C | |
| Blackbody radiance | $L(\lambda,T_s)$ | 6.85E−08 | 2.64E−05 | 7.97E−04 | 6.85E−08 | 2.64E−05 | 7.97E−04 |
| Surface-emitted radiance | $\varepsilon(\lambda)L(\lambda,T_s)$ | 6.50E−08 | 2.50E−05 | 7.57E−04 | 6.50E−08 | 2.50E−05 | 7.57E−04 |
| At-sensor radiance from surface emission | $L_S(\lambda)$ | 5.99E−08 | 2.11E−05 | 6.39E−04 | 5.99E−08 | 2.12E−05 | 6.39E−04 |
| Total at-sensor radiance | $L(\lambda)$ | 1.06E−04 | 3.77E−05 | 7.39E−04 | 6.10E−08 | 2.31E−05 | 7.38E−04 |
| Brightness temperature (°C) | $T^*$ | 162.3 °C | 23.0 °C | 10.3 °C | 13.5 °C | 12.2 °C | 10.3 °C |
| At-sensor radiance contributions (%) | | | | | | | |
| At-sensor radiance from surface emission | $L_S(\lambda)$ | 0.1 | 56.0 | 86.6 | 98.1 | 91.3 | 86.6 |
| Atmospheric up-welling (at-sensor) | $L_U(\lambda)$ | 0.0 | 5.1 | 12.9 | 1.8 | 8.3 | 12.9 |
| Surface-reflected solar (at-sensor) | $L_{SR}(\lambda)$ | 81.4 | 34.2 | 0.0 | 0.0 | 0.0 | 0.0 |
| Surface-reflected down-welling (at-sensor) | $L_{AR}(\lambda)$ | 0.0 | 0.2 | 0.5 | 0.1 | 0.4 | 0.5 |
| Solar radiance scattered to the sensor | $L_{scat}(\lambda)$ | 18.6 | 4.5 | 0.0 | 0.0 | 0.0 | 0.0 |

Table 2.6a. *Contribution of atmospheric up-welling and surface reflected components to at-sensor radiance. Contributions are assessed for the SWIR (2.1–2.5 μm), MIR (3.5–4.0 μm) and TIR (10–12 μm) during the day when reflection and scattering of solar radiation occurs, and at night, when the solar contribution is absent. Transmissivities, $\tau(\lambda,\theta_S)$ and $\tau(\lambda)$, as well as atmospheric down-welling and up-welling components, $E_a(\lambda)$ and $L_U(\lambda)$, are obtained using MODTRAN. MODTRAN was run using a 1976 US Standard atmosphere with a vertical path from sea-level to space (zenith = 180°, observer height = 100 km), a $CO_2$ mixing ratio of 380 ppm·v and a flat emissivity for basalt. Radiance values given in bold are the dominant components within each waveband.*

| Contribution of atmospheric up-welling and surface reflected radiance to at-sensor radiance | | | | | | | |
|---|---|---|---|---|---|---|---|
| | | Day-time (W $cm^{-2}$ $sr^{-1}$ $\mu m^{-1}$) | | | Night-time (W $cm^{-2}$ $sr^{-1}$ $\mu m^{-1}$) | | |
| Source | Term/derivation | SWIR | MIR | TIR | SWIR | MIR | TIR |
| Inputs | | | | | | | |
| Solar zenith angle (°)* | $\theta_S$ | | 23° | | | No Sun | |
| Surface emissivity | $\varepsilon(\lambda)$ | | 0.95 | | | 0.95 | |
| Surface albedo | $\rho(\lambda)$ | | 0.05 | | | No reflection (night-time) | |
| Surface-incident radiance | | | | | | | |
| TOA solar irradiance | $E_{TOA}(\lambda)$ | 2.21E−03 | 3.94E−04 | 6.66E−06 | | No solar irradiance (night-time) | |
| Transmissivity for in-coming $E_{TOA}(\lambda)$ | $\tau(\lambda,\theta_S)$ | 0.92 | 0.84 | 0.84 | | n/a | |
| Surface-incident solar radiance | $E_{in}(\lambda)$ | 1.87E−03 | 3.04E−04 | 5.18E−06 | | No surface-incident solar radiance | |
| Surface-incident down-welling radiance** | $E_a(\lambda)$ | 1.08E−09 | 1.93E−06 | 9.52E−05 | 1.57E-09 | 2.37E−06 | 9.52E−05 |
| At-sensor radiance components | | | | | | | |
| Transmissivity for up-welling radiance | $\tau(\lambda)$ | 0.92 | 0.84 | 0.84 | 0.91 | 0.85 | 0.84 |
| Atmospheric up-welling (at-sensor) | $L_U(\lambda)$ | 1.08E−09 | 1.93E−06 | **9.52E−05** | **1.08E−09** | **1.93E−06** | **9.52E−05** |
| Surface-reflected solar (at-sensor) | $L_{SR}(\lambda)$ | **8.62E−05** | **1.29E−05** | 2.19E−07 | 0.00E−00 | 0.00E−00 | 0.00E−00 |
| Surface-reflected down-welling (at-sensor) | $L_{AR}(\lambda)$ | 4.98E−11 | 8.13E−08 | 4.02E−06 | 4.98E−11 | 8.13E−08 | 4.02E−06 |
| Solar radiance scattered to the sensor | $L_{scat}(\lambda)$ | **1.97E-05** | 1.71E-06 | 1.33E-08 | 0.00E-00 | 0.00E-00 | 0.00E-00 |

* At mid-day, on 1 January at 0° N, 0° E.

** Following Singh and Warren (1983), $E_a(\lambda) = L_U(\lambda)$.

Table 2.6d. *Assessment of total radiance arriving at the satellite, the brightness temperature that this gives, and the contribution of each of the radiance sources to L(λ). Model is run for day-time conditions for surfaces at a range of temperatures (from 50 °C to 500 °C) emitting in the MIR (3.5–4.0 μm) and TIR (10–12 μm). We use an emissivity of 0.95 with the atmospheric up-welling and surface reflected contributions of Table 2.6a.*

| Daytime emission in the MIR & TIR (radiance in W $cm^{-2}$ $sr^{-1}$ $\mu m^{-1}$) | | | | | | | | |
|---|---|---|---|---|---|---|---|---|
| | $T_s$= 50 °C, $\varepsilon(\lambda)$ = 0.95 | | $T_s$= 100 °C, $\varepsilon(\lambda)$ = 0.95 | | $T_s$= 250 °C, $\varepsilon(\lambda)$ = 0.95 | | $T_s$= 500 °C, $\varepsilon(\lambda)$ = 0.95 | |
| Source | MIR | TIR | MIR | TIR | MIR | TIR | MIR | TIR |
| Surface temperature (°C) | 50 °C | 50 °C | 100 °C | 100 °C | 250 °C | 250 °C | 500 °C | 500 °C |
| Blackbody radiance | 1.12E−04 | 1.31E−03 | 5.48E−04 | 2.29E−03 | 1.05E−02 | 6.60E−03 | 1.13E−01 | 1.67E−02 |
| Surface-emitted radiance | 1.06E−04 | 1.25E−03 | 5.20E−04 | 2.17E−03 | 9.94E−03 | 6.27E−03 | 1.07E−01 | 1.58E−02 |
| At-sensor radiance from surface emission | 8.94E−05 | 1.05E−03 | 4.39E−04 | 1.83E−03 | 8.39E−03 | 5.30E−03 | 9.05E−02 | 1.34E−02 |
| Total at-sensor radiance | 1.06E−04 | 1.15E−03 | 4.56E−04 | 1.93E−03 | 8.40E−03 | 5.40E−03 | 9.05E−02 | 1.35E−02 |
| Brightness temperature (°C) | 48.6 | 40.1 | 93.4 | 83.4 | 234.8 | 213.6 | 467.2 | 426.7 |
| At-sensor radiance contributions (%) | | | | | | | | |
| At-sensor radiance from surface emission | 84.3 | 91.4 | 96.4 | 94.9 | 99.8 | 98.2 | 100.0 | 99.3 |
| Atmospheric up-welling (at-sensor) | 1.8 | 8.3 | 0.4 | 4.9 | 0.0 | 1.8 | 0.0 | 0.7 |
| Surface-reflected solar (at-sensor) | 12.2 | 0.0 | 2.8 | 0.0 | 0.2 | 0.0 | 0.0 | 0.0 |
| Surface-reflected down-welling (at-sensor) | 0.1 | 0.3 | 0.0 | 0.2 | 0.0 | 0.1 | 0.0 | 0.0 |
| Solar radiance scattered to the sensor | 1.6 | 0.0 | 0.4 | 0.0 | 0.0 | 0.0 | 0.0 | 0.0 |
| Basic correction for $\varepsilon(\lambda)$ and $\tau(\lambda)$ | | | | | | | | |
| Emissivity | 0.95 | 0.95 | 0.95 | 0.95 | 0.95 | 0.95 | 0.95 | 0.95 |
| Transmissivity | 0.84 | 0.84 | 0.84 | 0.84 | 0.84 | 0.84 | 0.84 | 0.84 |
| Corrected radiance (W $cm^{-2}$ $sr^{-1}$ $\mu m^{-1}$)[a] | 1.32E−04 | 1.44E−03 | 5.69E−04 | 2.41E−03 | 1.05E−02 | 6.73E−03 | 1.13E−01 | 1.68E−02 |
| Temperature (°C)[b] | 54.7 | 57.2 | 101.4 | 105.5 | 250.1 | 253.6 | 500.0 | 502.8 |

[a] Radiance obtained by correcting at-sensor radiance by just $\varepsilon(\lambda)$ and $\tau(\lambda)$.

[b] Temperature obtained from correcting at-sensor radiance by just $\varepsilon(\lambda)$ and $\tau(\lambda)$.

Table 2.6c. *Assessment of total radiance arriving at the satellite, the brightness temperature that this gives, and the contribution of each of the radiance sources to L(λ). Model is run for day-time emission in the SWIR for surfaces at a range of temperatures emitting in the SWIR (2.1–2.5 μm) between 100 °C and 1000 °C. We use an emissivity of 0.95 with the atmospheric up-welling and surface reflected contributions of Table 2.6a.*

| Day-time emission in the SWIR | | | | | | | |
|---|---|---|---|---|---|---|---|
| | | Radiance (W $cm^{-2}$ $sr^{-1}$ $\mu m^{-1}$) | | | | | |
| Source | Term/derivation | SWIR | SWIR | SWIR | SWIR | SWIR | SWIR |
| Surface temperature (°C) | $T_S$ | 100 °C | 250 °C | 375 °C | 500 °C | 750 °C | 1000°C |
| Blackbody radiance | $L(\lambda,T_S)$ | 9.64E−06 | 1.18E−03 | 1.19E−02 | 5.65E−02 | 4.09E−01 | 1.37E+00 |
| Surface-emitted radiance | $\varepsilon(\lambda)L(\lambda,T_S)$ | 9.16E−06 | 1.12E−03 | 1.13E−02 | 5.37E−02 | 3.89E−01 | 1.30E+00 |
| At-sensor radiance from surface emission | $L_S(\lambda)$ | 8.43E−06 | 1.03E−03 | 1.04E−02 | 4.94E−02 | 3.58E−01 | 1.20E+00 |
| Total at-sensor radiance | $L(\lambda)$ | 1.14E−04 | 1.14E−03 | 1.05E−02 | 4.95E−02 | 3.58E−01 | 1.20E+00 |
| Brightness temperature (°C) | $T^*$ | 164.6 | 248.4 | 366.8 | 487.6 | 728.2 | 966.5 |
| At-sensor radiance contributions (%) | | | | | | | |
| At-sensor radiance from surface emission | $L_S(\lambda)$ | 7.4 | 90.7 | 99.0 | 99.8 | 100.0 | 100.0 |
| Atmospheric up-welling (at-sensor) | $L_U(\lambda)$ | 0.0 | 0.0 | 0.0 | 0.0 | 0.0 | 0.0 |
| Surface-reflected solar (at-sensor) | $L_{SR}(\lambda)$ | 75.4 | 7.6 | 0.8 | 0.2 | 0.0 | 0.0 |
| Surface-reflected down-welling (at-sensor) | $L_{AR}(\lambda)$ | 0.0 | 0.0 | 0.0 | 0.0 | 0.0 | 0.0 |
| Solar radiance scattered to the sensor | $L_{scat}(\lambda)$ | 17.2 | 1.7 | 0.2 | 0.0 | 0.0 | 0.0 |
| Basic correction for $\varepsilon(\lambda)$ and $\tau(\lambda)$ | | | | | | | |
| Emissivity | $\varepsilon(\lambda)$ | 0.95 | 0.95 | 0.95 | 0.95 | 0.95 | 0.95 |
| Transmissivity | $\tau(\lambda)$ | 0.92 | 0.92 | 0.92 | 0.92 | 0.92 | 0.92 |
| Corrected radiance (W $cm^{-2}$ $sr^{-1}$ $\mu m^{-1}$)[a] | $L(\lambda)/[\varepsilon(\lambda)\,\tau(\lambda)]$ | 1.31E−04 | 1.30E−03 | 1.20E−02 | 5.66E−02 | 4.09E−01 | 1.37E+00 |
| Temperature (°C)[b] | $T^*$ | 168.7 | 254.2 | 375.7 | 500.2 | 750.0 | 1000.0 |

[a] Radiance obtained by correcting at-sensor radiance by just $\varepsilon(\lambda)$ and $\tau(\lambda)$.

[b] Temperature obtained from correcting at-sensor radiance by just $\varepsilon(\lambda)$ and $\tau(\lambda)$.

temperature that is ~65 °C higher than the actual surface temperature (c.f., $T_s$ and $T^*$ in Table 2.6c). As we move to 250 °C, the contribution of surface-emitted radiance to the total increases to 91%. The contribution of the reflected component is no longer sufficient to balance the effect of atmospheric attenuation, so the brightness temperature is now lower than the actual surface temperature by ~2 °C. As we move to higher temperatures, so the contribution of the reflected component to the total continues to decline, to approach 0% of the total at a surface temperature of 500 °C. As a result, attenuated surface-emitted radiance becomes the dominant source, attenuation meaning that the brightness temperature continues to be somewhat (~34 °C) less than the actual surface temperature.

For an ambient surface radiating at 15 °C in the MIR, the same model shows that 56% of the at-sensor radiance will be due to emission from the surface (Table 2.6b). Of the remainder, reflected and scattered solar radiation together contribute ~39% and atmospheric up-welling radiance contributes ~5%. The result is a brightness temperature that is ~8 °C higher than the actual surface temperature (c.f., $T_s$ and $T^*$ in Table 2.6b). By night, the solar source is absent, with surface emission accounting for more than 90% of the total at-sensor radiance, with atmospheric up-welling radiance contributing the remainder. Attenuation effects now dominate, so that the brightness temperature is ~3 °C lower than the actual surface temperature by night. As we increase the surface temperature, as in the Table 2.6d model, so the contribution of surface emission to the total at-sensor radiance becomes increasingly dominant, to approach 100% at a source temperature of 250 °C. However, the ever-present attenuation effect continues to modify the sensor-arriving radiance, so that the brightness temperature remains lower than the actual surface temperature by up to 33 °C (as in the 500 °C case of Table 2.6d).

In the TIR, Table 2.6b shows that the contribution of reflected and scattered solar radiation is small, having a combined contribution of <0.5% in all cases. The contribution of reflected down-welling radiance is also trivial in this low-reflectivity model. Instead, surface emission contributes more than 90% of the at-sensor radiance by both day and night, with atmospheric up-welling radiance contributing the remainder. Attenuation effects thus dominate so that the brightness temperature is lower than the surface temperature in all cases (c.f., $T_s$ and $T^*$ in Table 2.6d). As we increase the surface temperature, as in the Table 2.6d model, so the contribution of surface emission to the total at-sensor radiance becomes increasingly dominant, to exceed 99% at a source temperature of 500 °C. However, as in the MIR, attenuation effects result in brightness temperatures that are lower, by up to 73 °C, than the actual surface temperature.

Comparison of the surface temperature with the brightness temperature in Tables 2.6b and 2.6c shows that, if we use brightness temperature, we tend to under- or over-estimate true surface temperature. Atmospheric correction must, therefore, be completed if we are to extract surface temperature.

### *2.3.4 Variation in atmospheric up-welling and reflected solar radiation with altitude and scan angle*

The Table 2.6 model was run for a fixed path length, from a satellite vertically over the measurement point to sea-level. However, as with transmissivity, the quantity of up-welling

radiance and reflected solar radiance varies with path length, altitude and scan angle. For up-welling radiances, while longer path lengths contain a greater amount of atmosphere, so that more emitted radiance can be produced, thinner atmospheres above surfaces at higher altitudes result in lower amounts of atmospheric emission. At the same time, increased path lengths will result in increased absorption of surface arriving, and reflected, solar radiation, hence reducing the reflected solar radiation component arriving at the sensor. On the other hand, solar radiation passing through thinner atmospheres at higher altitudes will experience decreased absorption, hence increasing the amount of reflected solar radiation arriving at the sensor.

As plotted in Figure 2.17a, for a satellite sensor viewing the surface from a vantage point vertically above the surface, up-welling radiance will decrease with increased surface

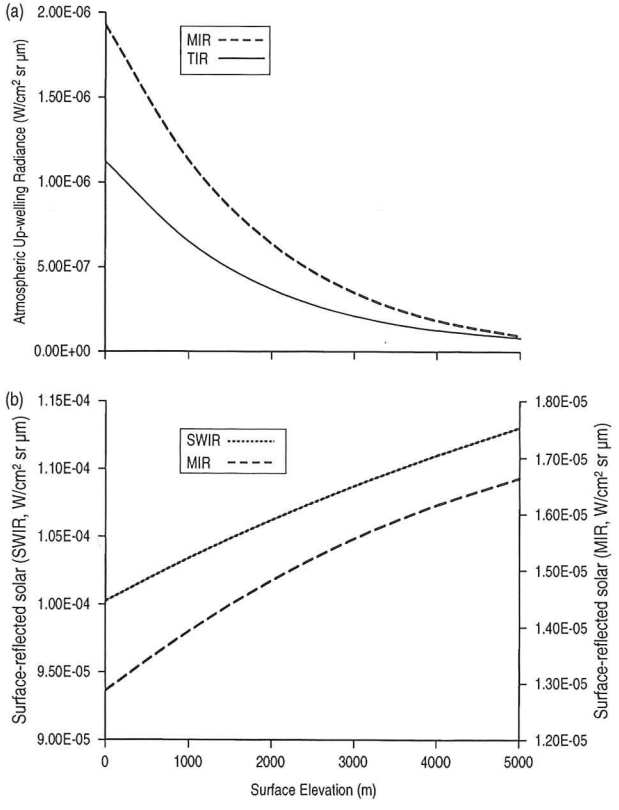


Figure 2.17 (a) Decrease in atmospheric up-welling radiance with surface elevation for a satellite viewing the surface from space in (i) the MIR (3.5–4.0 µm), and (ii) the TIR (10–12 µm). (b) Increase in surface-reflected radiance with surface elevation for a satellite viewing the surface from space in (i) the SWIR (2.1–2.5 µm), and (ii) the MIR (3.5–4.0 µm). The same MODTRAN US Standard atmosphere as used in Figure 2.14 is applied, and reflection is calculated (for mid day, on 1 January at 0° N, 0° E) following the procedure detailed in Appendix B.

elevation. This is a result of a reduction in the length of the atmospheric column between the surface and the sensor with elevation. Conversely, reflected solar radiation will increase with surface elevation (Figure 2.17b), a result of increased transmissivities with shorter path lengths and a thinner atmosphere. For a given surface elevation, although up-welling radiance will increase with scan angle, as the path length increases (Figure 2.18), reflected solar radiation will decrease due to increased absorption along the longer path length (Figure 2.19).

So far we have considered reflection from a high-emissivity (basaltic) surface. Of course, reflected solar radiation will increase with surface reflection in the SWIR and MIR, i.e., as emissivity decreases, reflected solar radiation increases (Figure 2.20a). Reflected atmospheric down-welling radiance in the MIR and TIR will also increase as surface reflection increases (Figure 2.21). At the same time, reflected solar radiation will decrease with solar

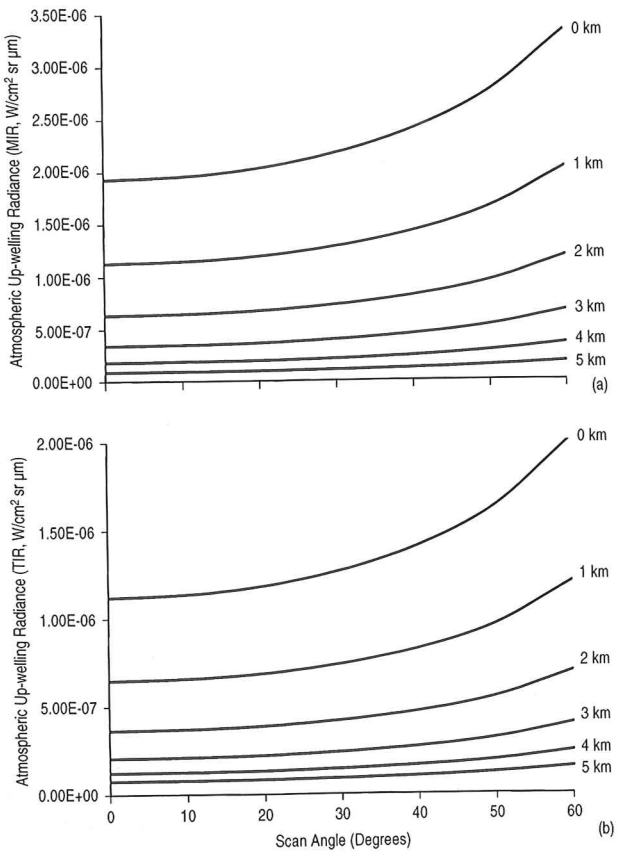


Figure 2.18 Variation in atmospheric up-welling radiance with scan angle and surface elevation for a satellite viewing the surface from space in (a) the MIR (3.5–4.0 μm), and (b) the TIR (10–12 μm). The same MODTRAN US Standard atmosphere as used in Figure 2.14 is applied.

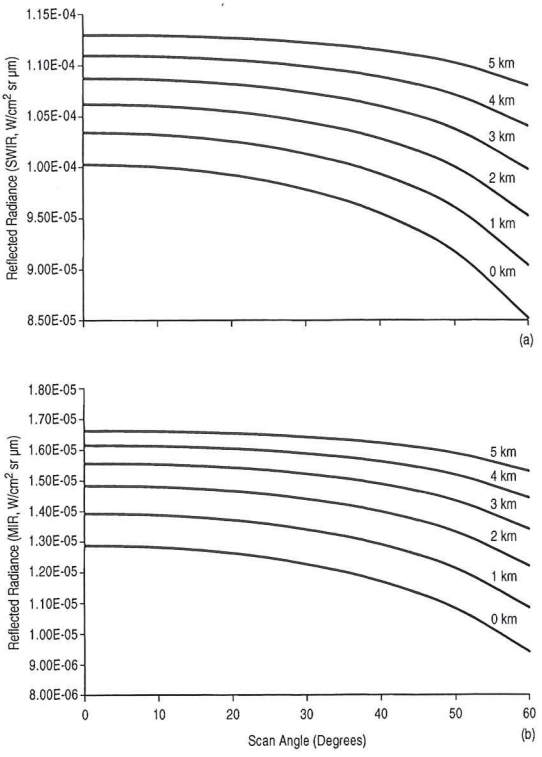


Figure 2.19 Variation in surface-reflected radiance with scan angle and surface elevation for a satellite viewing the surface from space in (a) the SWIR (2.1–2.5 μm), and (b) the MIR (3.5–4.0 μm). The same MODTRAN US Standard atmosphere as used in Figure 2.14 is applied.

zenith angle, declining from a maximum when the Sun is directly overhead, so that $\theta_S = 0$, to a minimum when the Sun is lower in the sky ($\theta_S > 0$) (Figure 2.20b).

### 2.3.5 Atmospheric correction

If we consider the transmissive and emissive effects of the atmosphere, as well as the reflective and emissive properties of the surface, an equation for the effects of atmospheric emission, absorption and surface reflection on the sensor-arriving radiance can be written. Taking Equation (2.14b) and writing $L_S(\lambda)$ in full we obtain:

$$L(\lambda)^* = L(\lambda, T^*) = \tau(\lambda)\, \varepsilon(\lambda)\, L(\lambda, T_s) + L_U(\lambda) + L_R(\lambda). \quad (2.21a)$$

Re-arranging shows that surface temperature ($T_s$) can be obtained from the brightness temperature through:

$$L(\lambda, T_s) = [L(\lambda, T^*) - L_U(\lambda) - L_R(\lambda)] \,/\, [\tau(\lambda)\, \varepsilon(\lambda)]. \quad (2.21b)$$

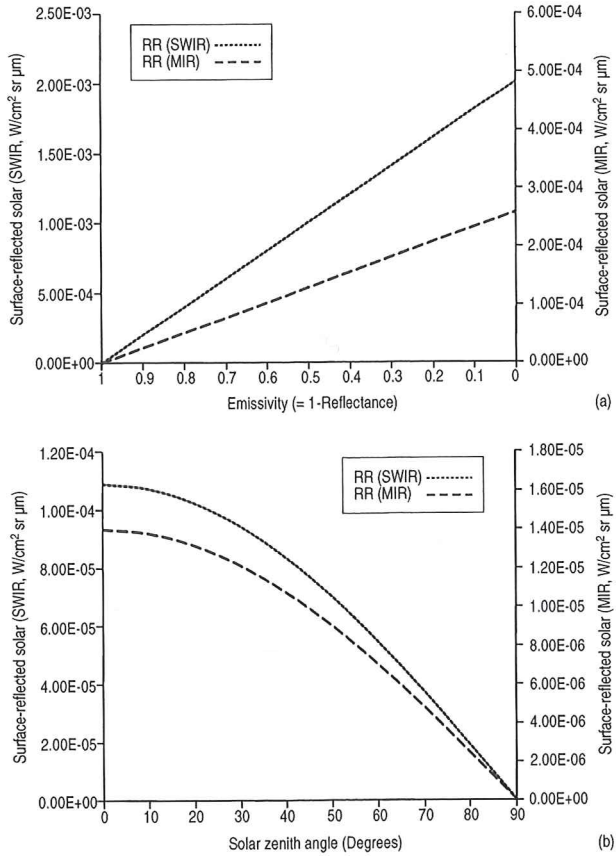


Figure 2.20 Variation in surface reflected radiance in the SWIR (left-hand axis) and MIR (right-hand axis) with (a) surface emissivity and (b) solar zenith angle. The same MODTRAN US Standard atmosphere as used in Figure 2.14 is applied, and reflection is calculated following the procedure detailed in Appendix B.

As we know, parameter $L_R(\lambda)$ is composed of three components. Writing each of the terms of Equation (2.15) in full shows that the reflected component of the sensor-arriving radiance is itself described by:

$$L_R(\lambda) = \tau(\lambda)\,[1 - \varepsilon(\lambda)]\,\{\tau(\lambda, \theta_S)\,[E_{TOA}(\lambda) + E_{sp}(\lambda)] + L_U(\lambda)\}. \qquad (2.21c)$$

Equations (2.21b) and (2.21c), in effect, describe the atmospheric correction that we need to apply to the sensor-recorded radiance if we are to isolate the quantity we require, i.e., $L(\lambda,T_S)$. That is, if we are to arrive at the true surface kinetic temperature, we have to subtract the atmospheric up-welling and reflected components from the at-satellite radiance, and then divide by transmissivity and emissivity.

We can simplify matters if we consider the importance of each term within each of the atmospheric windows of interest, and reject those that do not significantly contribute to the

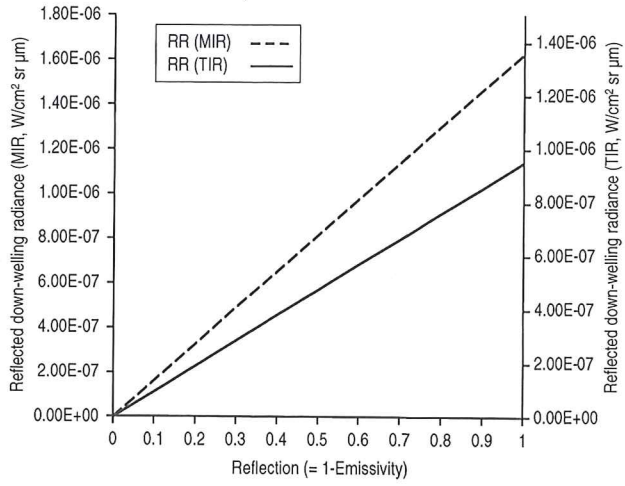


Figure 2.21 Increase in surface-reflected down-welling radiance in the MIR (left-hand axis) and TIR (right-hand axis) with surface reflection. The same MODTRAN US Standard atmosphere as used in Figure 2.14 is applied.

total at-sensor radiance. First, though, we can remove one component. Reflected space radiance is extremely small at all infrared wavelengths. Thus we can discount $E_{sp}(\lambda)$ for all cases and simplify Equation (2.21c) to:

$$L_R(\lambda) = \tau(\lambda)\,[1 - \varepsilon(\lambda)]\,[\tau(\lambda, \theta_S)\,E_{TOA}(\lambda) + L_U(\lambda)]. \quad (2.22)$$

### 2.3.5.1 *Atmospheric correction in the SWIR*

As can be seen by examining the cases in Table 2.6c, reflection of atmospheric down-welling radiance makes a negligible contribution to the total at-satellite radiance in the SWIR, as does atmospheric up-welling radiance. As a result, Equation (2.21b) can be simplified to

$$L(\lambda, T_s) = [L(\lambda, T^*) - L_R(\lambda)] \,/\, [\tau(\lambda)\varepsilon(\lambda)] \quad (2.23a)$$

and (2.22) to:

$$L_R(\lambda) = \tau(\lambda)\,[1 - \varepsilon(\lambda)]\,[\tau(\lambda, \theta_S)\,E_{TOA}(\lambda)]. \quad (2.23b)$$

In other words, we only have to correct the at-sensor signal for reflection of solar radiation and atmospheric attenuation. However, solar radiance scattered upwards towards the sensor by the atmosphere contributes up to 15% of the total at-sensor radiance, so that the contribution of back-scattered radiation, $L_{scat}(\lambda)$, needs to be added to Equation (2.23b):

$$L_R(\lambda) = \tau(\lambda)\,[1 - \varepsilon(\lambda)][\tau(\lambda, \theta_S)\,E_{TOA}(\lambda)] + L_{scat}(\lambda). \quad (2.23c)$$

Thus, the atmospheric correction in the SWIR involves making an estimate for, and subtracting, the contributions of reflected and scattered solar radiation, as well as atmospheric transmissivity, in:

$$L(\lambda, T_s) = [L(\lambda, T^*) - L_R(\lambda) - L_{scat}(\lambda)] / [\tau(\lambda)\varepsilon(\lambda)]. \quad (2.24a)$$

Typical values for $L_R(\lambda)$, $L_{scat}(\lambda)$ and $\tau(\lambda)$ are given, for a path length from space to sea-level, in Table 2.6a. Of course, as shown in Table 2.6a, at night there is no solar reflected or scattered contribution, so that the correction reduces to:

$$L(\lambda, T_s) = L(\lambda, T^*) / [\tau(\lambda)\varepsilon(\lambda)]. \quad (2.24b)$$

In fact, examination of Table 2.6c shows that by day, for low-reflectivity surfaces ($\rho(\lambda) <$ 5%), once the temperature of the surface exceeds 350 °C, surface emission accounts for more than 99 % of the total at-sensor radiance. As a result, under such conditions, Equation (2.24b) may be applied to day time data to approximate surface temperature from brightness temperature. This correction is sufficient to retrieve surface temperatures to within 0.2 °C for surfaces at 500 °C. However, for cooler surfaces the failure to remove the reflected component will result in an over-estimate of surface temperature by between 1 °C and 68 °C, as can be seen by comparing $T_s$ and $T^*$ in Table 2.6c.

### 2.3.5.2 *Atmospheric correction in the TIR*

As can be seen by examining the cases in Table 2.6d, reflection and scattering of solar radiation makes a negligible contribution to the total at-satellite radiance in the TIR. Instead, atmospheric up-welling radiance can contribute as much as 13% to the total at sensor radiance. As a result, Equation (2.21b) can be simplified to

$$L(\lambda, T_s) = [L(\lambda, T^*) - L_U(\lambda)] / [\tau(\lambda)\varepsilon(\lambda)] \quad (2.25)$$

In other words, we only have to correct the at-sensor signal for atmospheric up-welling radiation and atmospheric attenuation. Typical values for $L_U(\lambda)$ and $\tau(\lambda)$, for a path length from sea-level to space are given in Table 2.6a. Table 2.6d shows that the relative contribution of $L_U(\lambda)$ to the total at-satellite radiance decreases as surface temperature increases, declining to 0.7% of the total when considering emission from surfaces at 500 °C. However, even at 500 °C, failure to remove the atmospheric up-welling component will result in an over-estimate of surface temperature by ~3 °C (compare $T_s$ and $T^*$ in Table 2.6d).

### 2.3.5.3 *Atmospheric correction in the MIR*

The at-sensor radiance in the MIR is complicated by solar radiance reflected from the surface and back-scattered by the atmosphere, as well as by the presence of atmospheric up-welling radiance. As can be seen from Table 2.6b, reflected solar radiation is the

dominant radiance contribution to the total at-sensor radiance after surface emission, representing ~34% of the total at-sensor radiance over ambient surfaces. However, scattered and up-welling radiance contribute ~4% and 6% of the total, respectively. Thus, correction in the MIR is the most complicated of the three cases, requiring correction for the contributions of reflected, scattered and up-welling radiance, while taking into account the effects of attenuation, so that:

$$L(\lambda, T_s) = [L(\lambda, T^*) - L_U(\lambda) - L_R(\lambda)] / [\tau(\lambda)\varepsilon(\lambda)], \quad (2.26a)$$

in which

$$L_R(\lambda) = \tau(\lambda)\,[1 - \varepsilon(\lambda)][\tau(\lambda, \theta_S)\, E_{TOA}(\lambda)] + L_{scat}(\lambda). \quad (2.26b)$$

Examination of Table 2.6b shows that, over ambient surfaces, only the contribution of reflected down-welling atmospheric radiance can be neglected. By night, the solar-reflected and scattered components can also be neglected (Table 2.6b), so that Equation (2.26) simplifies to:

$$L(\lambda, T_s) = [L(\lambda, T^*) - L_U(\lambda)] / [\tau(\lambda)\varepsilon(\lambda)]. \quad (2.26c)$$

Table 2.6c shows that, by day, the same is true once the surface temperature exceeds 100 °C, if the reflectivity of the surface is low ($\rho(\lambda) < 5\%$). Also, as the temperature of the surface reaches ~250 °C, so the contribution of $L_U(\lambda)$ declines to less than 0.5% of the total. Over low-reflectivity (basaltic) surfaces, and at surface temperatures of greater than 250 °C, $T_s$ can therefore be approximated from:

$$L(\lambda, T_s) = L(\lambda, T^*) / [\tau\,(\lambda)\,\varepsilon\,(\lambda)]. \quad (2.27)$$

Comparing $T_s$ and $T^*$ in Table 2.6d shows that, for a surface temperature of 250 °C, this will return a corrected temperature of 250.1 °C.

## 2.4 Brightness temperature and surface temperature: how to obtain surface temperature

An overview of the steps required to determine a surface temperature from satellite sensor data is given in Cracknell (1997). It is given, in modified form, here in Figure 2.22.

### *2.4.1 A summary of the physical processes controlling at-sensor radiance*

The left-hand side of Figure 2.22 illustrates the physical principles involved in transmitting the radiance from the surface to the satellite sensor. These are as follows.

(1) Radiation is emitted by the surface, its spectral distribution being governed by the Planck Function, modified by emissivity. Radiation is also reflected from the surface, the intensity depending on the wavelength of the measurement, the level of incoming solar radiation and the reflectivity of the surface.

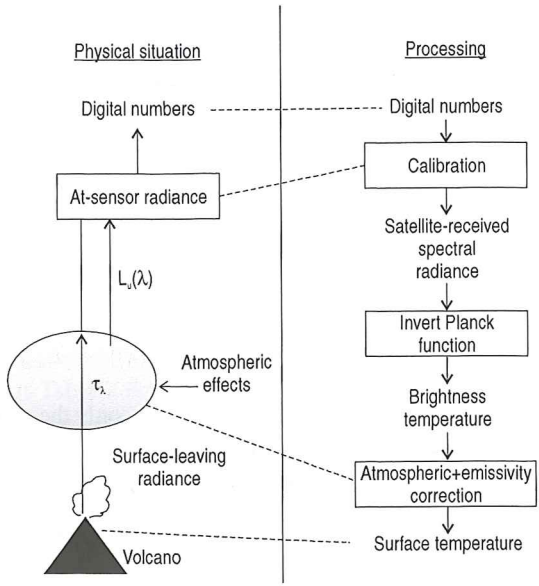


Figure 2.22 Summary of the physical processes affecting surface-leaving spectral radiance during its passage from the surface to the space-based sensor (left-hand side), with the processing required to retrieve the surface kinematic temperature from the satellite-sensor recorded digital number on the right-hand side [modified from Cracknell (1997, Fig. 4.3)].

(2) The radiation travels upwards to the space-based sensor, passing through the entire atmospheric column. The atmosphere itself emits further radiation, while absorbing some of the surface-emitted and -reflected radiation.

(3) The radiation arrives at the satellite where it registers a voltage on the detector proportional to the level of at-sensor radiance. The voltage is converted to a digital number (DN), which is usually related to incident, at-sensor, radiance ($R^*$) through a linear relationship, whereby:

$$R^* = a\,DN + b, \tag{2.28}$$

in which $a$ and $b$ are known calibration coefficients (see Electronic Supplement 2).

(4) This, through inversion of the Planck Function, can be converted to a brightness temperature ($T^*$) through

$$T^* = \frac{c_2}{\lambda \ln\left(\frac{c_1 \lambda^{-5}}{R^*} + 1\right)}. \tag{2.29}$$

### 2.4.2 *Processing of at-sensor radiance to obtain surface-leaving radiance*

The right-hand side of Figure 2.22 outlines the processing operations required to invert the process and thereby convert the satellite-recorded value (the DN), back to the desired quantity (surface temperature). The main steps are as follows.

(1) Cloud detection and elimination.
(2) Conversion of the DN to at-sensor radiance through application of Equation (2.28).
(3) Correction of the at-satellite radiance ($R_{in}$*) for atmospheric and emissivity effects using, for the SWIR:

$$L(\lambda, T_s) = [R_{in}^* - L_R(\lambda) - L_{scat}(\lambda)] / [\tau(\lambda)\, \varepsilon(\lambda)] \tag{2.30a}$$

for the MIR:

$$L(\lambda, T_s) = [R_{in}^* - L_U(\lambda) - L_R(\lambda)] / [\tau(\lambda)\, \varepsilon(\lambda)] \tag{2.30b}$$

and for the TIR:

$$L(\lambda, T_s) = [R_{in}^* - L_U(\lambda)] / [\tau(\lambda)\, \varepsilon(\lambda)]. \tag{2.30c}$$

(4) Finally, the Planck Function is inverted and the atmospherically and emissivity corrected radiance [$R = L(\lambda,T_s)$] is used (with the appropriate wavelength) to obtain surface temperature from:

$$T_s = \frac{c_2}{\lambda \ln\left(\frac{c_1 \lambda^{-5}}{R} + 1\right)}. \tag{2.30d}$$

This process is considered in more detail in Electronic Supplement 3 where, to obtain an exact temperature for a selective radiator, the sensor spectral response function may have to be convolved with spectral emissivity and transmissivity. However, as shown in Electronic Supplement 3, a good approximation of surface temperature (theoretically to within 0.1 °C) can be obtained by following the above steps and inputting appropriate band-averaged values. Band-averaged emissivity, atmospheric and reflection correction values for some commonly used sensors and wavebands are given in Electronic Supplement 4.

## 2.5 Summation

Here we define precision and accuracy. Precision is the degree of refinement with which we can make a measurement, i.e., to how many significant figures can we make the measurement? For a remote sensing sensor this can be defined by the noise equivalent temperature difference ($NE\Delta T$), i.e., the variation in measured temperature due to detector noise (see Section 3.4.2 of Chapter 3). This is typically less than 0.5 °C for most satellite-based thermal detectors. This contrasts with accuracy, which is the degree to which the measurement conforms to the truth. In our case, we need to ask how close is the measurement of surface temperature, as derived from the integrated radiance recorded by the detector, to the actual surface temperature?

Over a surface of homogeneous temperature (at pixel scale), it is unlikely that we can execute emissivity and atmospheric correction to allow estimation of surface temperature to

an accuracy any greater than 1 °C. Over an active lava the problem can be exacerbated by extreme heterogeneity in surface temperature at the scale of the pixel, requiring application of mixture models to extract actual surface temperature (see Chapter 4). The presence of volcanic gas will also complicate the problem (see Section 9.4.6.7 of Chapter 9). Thus, in the absence of precise atmospheric and emissivity data specific to the time and location of the measurement, accuracies of a few degrees centigrade are (have to be) acceptable. Comparisons between actual surface temperature and those obtained from a satellite-based measurement are given in Electronic Supplement 4.